Effect of permeability anisotropy on buoyancy-driven flow for CO_2 sequestration in saline aquifers

Philip Cheng,[1] Michael Bestehorn,[2] and Abbas Firoozabadi[1,3]

[1] Solubility trapping of carbon dioxide (CO_2) in deep saline aquifers is considered one of the most effective methods for carbon sequestration. Dissolution of CO_2 into the brine may create gravitational instabilities that lead to the onset of convection, which greatly enhances the storage efficiency and reduces the possibilities of leakage. Convection appears in the form of downward traveling fingers of relatively dense, CO_2-dissolved fluid. Many natural aquifer formations display considerable permeability anisotropy, where the horizontal permeability k_h may be several times greater than the vertical permeability k_z. It has been previously found that increasing k_h for a fixed k_z reduces the critical time t_c at which onset occurs and the critical wavelength λ_c with which the fingers initially form. We extend earlier work by showing how and why this occurs. Our results reveal new insights about λ_c. We have studied the behavior for times greater than t_c using high-resolution numerical simulations. We show that the enhanced dissolution from convection can become significant much earlier in anisotropic media. Furthermore, the effects of anisotropy may be sustained for a long period of time. Our results suggest that permeability anisotropy can allow a wider range of aquifer formations to be considered for effective sequestration.

1. Introduction

[2] Carbon sequestration in deep saline aquifers may be considered one of the most promising ways to mitigate rising atmospheric carbon dioxide (CO_2) levels [*Intergovernmental Panel on Climate Change* (*IPCC*), 2005; *Weir et al.*, 1996; *Lindeberg and Wessel-Berg*, 1997; *Ennis-King et al.*, 2005; *Xu et al.*, 2006; *Riaz et al.*, 2006; *Firoozabadi and Cheng*, 2010]. The idea is to capture CO_2 from stationary sources, such as coal-fired power plants, and store it in aquifers located deep beneath the Earth's surface. Aquifers are an attractive storage option because they are widely distributed around the world, and because the total pore volume is estimated to be large enough to store global CO_2 emissions for at least several decades [*IPCC*, 2005; *Firoozabadi and Cheng*, 2010]. The solubility of CO_2 in water is up to several mass percent. It is somewhat lower in brines. Initially after injection, the CO_2 will be transported into the brine below through diffusion only. However, dissolution of CO_2 increases the density of the resulting aqueous mixture, creating gravitational instabilities that may lead to convection. This so-called solubility trapping of the CO_2 is of special importance to the potential issue of CO_2 leakage back into the atmosphere [*IPCC*, 2005; *Weir et al.*, 1996; *Lindeberg and Wessel-Berg*, 1997; *Ennis-King et al.*, 2005; *Xu et al.*, 2006; *Riaz et al.*, 2006; *Firoozabadi and Cheng*, 2010]. Convection is manifested in the form of downward traveling 'fingers' of relatively dense, CO_2-dissolved fluid. It greatly enhances the rate of transport over diffusion alone and thereby increases the efficiency of the solubility trapping. Some natural formations may appear to be unsuitable for storage because of their low vertical permeability. However, many natural formations display considerable permeability anisotropy, where the horizontal permeability may be several times greater than the vertical permeability. If the horizontal permeability is sufficiently high, they could still potentially be attractive storage sites as long as the vertical permeability is not too low. Thus, our goal is to investigate and quantify the effect of the increased horizontal permeability on the convective mixing.

[3] A few authors have performed linear stability analyses to study the effect of permeability anisotropy on the onset of convection [*Ennis-King et al.*, 2005; *Xu et al.*, 2006; *Hong and Kim*, 2008; *Rapaka et al.*, 2009]. That is, they have examined the influence of anisotropy on the stability of a base state (the diffusion-only solution) with respect to perturbations that grow in time. The problem presents a formidable challenge because the base state is time dependent. Past works have focused on finding the critical time t_c at which onset occurs and the critical wavelength λ_c with which the fingers form upon onset. They are largely based on the work by Ennis-King et al., who themselves have applied

---

[1]Department of Chemical and Environmental Engineering, Yale University, New Haven, Connecticut, USA.
[2]Lehrstuhl für Theoretische Physik II, Brandenburgische Technische Universität Cottbus, Cottbus, Germany.
[3]Reservoir Engineering Research Institute, Palo Alto, California, USA.

Corresponding author: A. Firoozabadi, Department of Chemical and Environmental Engineering, Yale University, 9 Hillhouse Ave., New Haven, CT 06511, USA. (abbas.firoozabadi@yale.edu)

*The PDF is correct here. The article as it originally published appears online.

methods from past studies involving a time-dependent base state subject to a thermal gradient [*Foster*, 1965; *Caltagirone*, 1980]. All of the stability analyses solve an initial value problem in which a system of ordinary differential equations is integrated over time. Ennis-King et al. consider the situation where the horizontal permeability k_h is fixed while the vertical permeability k_z is varied and is always less than k_h. They have found that t_c and λ_c become larger as k_z decreases. Their results are encoded in scaling relations that show the dependence of t_c and λ_c on various fluid and porous medium properties (e.g., t_c scales linearly with the diffusion coefficient and with the square of the porosity). Xu et al. as well as Hong and Kim solve the equations in a similar way using the same initial condition and obtain nearly identical results. The nonmodal analysis introduced in an earlier work overcomes the need for an arbitrary initial condition [*Rapaka et al.*, 2008]. Nevertheless, this method produces very similar results as the others [*Rapaka et al.*, 2009].

[4] Despite the significant progress, many aspects have not yet been explored. As alluded to earlier, a more pertinent issue regarding anisotropy may be to study the effect of increasing k_h while keeping k_z fixed. This problem has been examined by *Xu et al.* [2006]. Their results are obtained purely through numerical curve fitting and are confined to scaling relations which show that t_c and λ_c become smaller with increasing anisotropy (higher values of k_h). They do not address how and why anisotropy makes the base state more unstable. Moreover, studies on the effect of anisotropy after the critical time are limited. The behavior for times greater than t_c is important for two main reasons. First, results from numerical simulations in isotropic media [*Hassanzadeh et al.*, 2007; *Pruess and Zhang*, 2008; *Pau et al.*, 2010; *Elenius and Johannsen*, 2012] and experiments in Hele-Shaw cells [*Kneafsey and Pruess*, 2010] suggest that there can be a large difference between the critical time and the time when the enhanced transport from convection becomes significant. This is because the velocities must grow to a certain extent before convection is able to substantially affect the dynamics. It would be of practical importance if anisotropy could reduce the gap between this time and the critical time. Second, we are interested in monitoring the extent to which anisotropy can enhance mixing and seeing if its impact can be long-lasting. An earlier work includes coarse-grid simulations of a low k_h (60 mdarcy) anisotropic formation where k_z ranges from 0.06 to 60 mdarcy [*Ennis-King and Paterson*, 2005]. However, the coarseness of the grids severely limits the applicability of the simulations. They are used only to verify that keeping k_h fixed while decreasing k_z does delay the time when convection becomes significant, as expected. High-resolution simulations have been performed for only isotropic media [*Riaz et al.*, 2006; *Hassanzadeh et al.*, 2007; *Pruess and Zhang*, 2008; *Hidalgo and Carrera*, 2009; *Pau et al.*, 2010; *Xie et al.*, 2011; *Elenius and Johannsen*, 2012].

[5] The central theme of this work is the effect of permeability anisotropy on the onset and subsequent development of convection. In particular, we consider the situation where k_z is fixed while k_h is increased. The paper is structured as follows. We describe the formulation in section 2. Our linear stability analysis, which is the focus of section 3, complements and extends previous work. We analyze the mechanism through which anisotropy causes the diffusion-only base state to become more unstable. In addition to deriving scaling relations which show that t_c and λ_c decrease with increasing anisotropy, we give physical and mathematical (analytical) reasoning for why this is so. Our results reveal new insights about the nature of the perturbations and the critical wavelength. We have studied the behavior for times greater than t_c through detailed two-dimensional (2-D) numerical simulations and present the results in section 4. We demonstrate the effect of anisotropy on three measures: CO₂ dissolution rates, convective/fingering velocities, and CO₂ concentration profiles. Our results show that the enhanced mixing from anisotropy can have a sustained impact lasting long after t_c. We conclude with some brief remarks.

2. Problem Formulation

2.1. Governing and Constitutive Equations

[6] We study isothermal fluid flow in a water-filled porous medium. The expressions in section 3 are simplest if we use a Cartesian coordinate system centered at the top boundary where the z direction is taken to be positive when pointing upward. The size of the medium may be specified by a height H in the z direction (z ranges from 0 to $-H$), a width W in the x direction, and a length L in the y direction. It is idealized to be nondeformable, inert, and homogeneous in its porosity ϕ and permeability. We consider an initial configuration where the pores are devoid of CO₂, except along the top boundary, where there is a thin, CO₂-saturated aqueous layer. Carbon dioxide is transported to this layer from above via dissolution from a CO₂ phase that acts as a large CO₂ reservoir. The layer always remains saturated with CO₂ at a fixed mass fraction ω_{sat}; it thus serves as a continual source of carbon dioxide in the porous domain. We ignore mass transfer of water into the CO₂ phase and capillary effects.

[7] We apply the Boussinesq approximation so that variations in the density ρ are neglected except when it appears in the gravity term. The fluid viscosity μ and the CO₂-H₂O diffusion coefficient D are treated as constants. The diffusive flux is given by Fick's law as $\mathbf{J} = -\phi D \rho \nabla \omega$, where ω is the CO₂ mass fraction. Fluid flow is governed by Darcy's law, the continuity equation, and a species balance for CO₂. They may be expressed, respectively, as

$$w = -\frac{k_z}{\mu}\left(\frac{\partial p}{\partial z} + \rho g\right), \tag{1}$$

$$u = -\frac{k_h}{\mu}\left(\frac{\partial p}{\partial x}\right), \tag{2}$$

$$v = -\frac{k_h}{\mu}\left(\frac{\partial p}{\partial y}\right), \tag{3}$$

$$\frac{\partial u}{\partial x} + \frac{\partial v}{\partial y} + \frac{\partial w}{\partial z} = 0, \tag{4}$$

$$\frac{\partial \omega}{\partial t} = -\frac{1}{\phi}\left(u\frac{\partial \omega}{\partial x} + v\frac{\partial \omega}{\partial y} + w\frac{\partial \omega}{\partial z}\right) + D\left(\frac{\partial^2 \omega}{\partial x^2} + \frac{\partial^2 \omega}{\partial y^2} + \frac{\partial^2 \omega}{\partial z^2}\right), \tag{5}$$

where p is the pressure, and u, v, w are the components of the Darcy velocity $\mathbf{q}$ in the x, y, and z directions, respectively. The permeability in the z direction is specified by k_z, while those in the x and y directions are specified by a horizontal permeability k_h, which may be different from the vertical

permeability k_z. All off-diagonal terms of the permeability tensor are zero. The density obeys the linear constitutive equation

$$\rho = \rho_0(1 + \alpha\omega). \tag{6}$$

Here, ρ_0 and α are constants. We denote the maximum increase in density from dissolution as $\Delta\rho = \rho_0\alpha\omega_{\text{sat}}$. Equation (6) plays an important role in previous studies [*Ennis-King et al.*, 2005; *Xu et al.*, 2006; *Riaz et al.*, 2006; *Hong and Kim*, 2008; *Rapaka et al.*, 2009], but it is used without theoretical justification. In Appendix A, we describe how (6) may be derived from basic thermodynamics. Its validity for this problem has also been verified experimentally [*Yang and Gu*, 2006]. Using (6) and letting $P = p + \rho_0 gz$, we may express (1) as

$$w = -\frac{k_z}{\mu}\left(\frac{\partial P}{\partial z} + \rho_0\alpha\omega g\right). \tag{7}$$

2.2. Nondimensionalization

[8] We use an adaptation of the nondimensionalization scheme discussed in a few earlier studies on isotropic media [*Riaz et al.*, 2006; *Hidalgo and Carrera*, 2009; *Slim and Ramakrishan*, 2010]. We define a velocity scale $\mho = k_z\Delta\rho g/\mu$, a length scale $\ell = \phi D/\mho = D\phi\mu/k_z\Delta\rho g$, and a timescale $\tau = \phi\ell/\mho = D(\phi\mu/k_z\Delta\rho g)^2$. Like in previous work [*Ennis-King et al.*, 2005; *Xu et al.*, 2006; *Hong and Kim*, 2008; *Rapaka et al.*, 2009], we also define an anisotropy ratio $\gamma = k_z/k_h$. In isotropic media, $\gamma = 1$. Using these quantities, we introduce the nondimensionalized variables

$$\langle\tilde{x}, \tilde{y}, \tilde{z}\rangle = \frac{1}{\ell}\left\langle\gamma^{1/2}x, \gamma^{1/2}y, z\right\rangle,$$

$$\langle\tilde{u}, \tilde{v}, \tilde{w}\rangle = \frac{1}{\mho}\left\langle\gamma^{1/2}u, \gamma^{1/2}v, w\right\rangle,$$

$$\tilde{t} = \frac{1}{\tau}t, \quad \tilde{\omega} = \frac{1}{\omega_{\text{sat}}}\omega, \quad \tilde{P} = \frac{1}{\Delta\rho g\ell}P.$$

Substituting these variables into (2)–(7), we obtain

$$\tilde{\mathbf{q}} = -\nabla\tilde{P} - \tilde{\omega}\nabla\tilde{z} \tag{8}$$

$$\nabla \cdot \tilde{\mathbf{q}} = 0, \tag{9}$$

$$\frac{\partial\tilde{\omega}}{\partial\tilde{t}} = -\tilde{\mathbf{q}} \cdot \nabla\tilde{\omega} + \gamma\left(\frac{\partial^2\tilde{\omega}}{\partial\tilde{x}^2} + \frac{\partial^2\tilde{\omega}}{\partial\tilde{y}^2}\right) + \frac{\partial^2\tilde{\omega}}{\partial\tilde{z}^2}, \tag{10}$$

where $\tilde{\mathbf{q}} = \langle\tilde{u}, \tilde{v}, \tilde{w}\rangle$ and $\nabla = \langle\partial/\partial\tilde{x}, \partial/\partial\tilde{y}, \partial/\partial\tilde{z}\rangle$ represents the dimensionless gradient operator. We define a Rayleigh number Ra as

$$\text{Ra} = \frac{H}{\ell} = \frac{\mho H}{\phi D} = \frac{k_z\Delta\rho gH}{\phi\mu D}. \tag{11}$$

In this choice of scaling, Ra appears only in the location of the bottom boundary. The concentration front will still be far away from the bottom at the onset of convection for sufficiently thick formations. The results from a linear stability analysis for such formations are independent of Ra, and hence are universal [*Slim and Ramakrishan*, 2010].

[9] We apply 2-D versions of (8)–(10) in the numerical simulations. For the purposes of simplifying the computations [*Tan and Homsy*, 1988; *Bestehorn*, 1993; *Riaz et al.*, 2006; *Rapaka et al.*, 2008], we express the velocity components in terms of a stream function $\psi = \psi(\tilde{x}, \tilde{z}, \tilde{t})$ that automatically satisfies (9):

$$\tilde{u} = \frac{\partial\psi}{\partial\tilde{z}}, \tag{12}$$

$$\tilde{w} = -\frac{\partial\psi}{\partial\tilde{x}}. \tag{13}$$

Taking the curl of (8) and using (12) along with (13), we obtain

$$\nabla^2\psi = \frac{\partial\tilde{\omega}}{\partial\tilde{x}}. \tag{14}$$

We can express the 2-D version of (10) in terms of ψ as

$$\frac{\partial\tilde{\omega}}{\partial\tilde{t}} = \frac{\partial\psi}{\partial\tilde{x}}\frac{\partial\tilde{\omega}}{\partial\tilde{z}} - \frac{\partial\psi}{\partial\tilde{z}}\frac{\partial\tilde{\omega}}{\partial\tilde{x}} + \gamma\frac{\partial^2\tilde{\omega}}{\partial\tilde{x}^2} + \frac{\partial^2\tilde{\omega}}{\partial\tilde{z}^2}. \tag{15}$$

Equations (14) and (15) constitute the form of the governing equations solved by the numerical simulations.

2.3. Boundary and Initial Conditions

[10] For both the stability analysis and the 2-D simulations, we use a no-flow condition through the top boundary ($\tilde{w} = 0$ at $\tilde{z} = 0$) and a no-flux condition through the impermeable bottom boundary ($\partial\tilde{\omega}/\partial\tilde{z} = \tilde{w} = 0$ at $\tilde{z} = -\text{Ra}$). The no-flow condition is commonly found in the CO$_2$ sequestration literature, and it essentially implies that the vertical convective flux between the top boundary and the CO$_2$ phase is negligible compared to the vertical diffusive flux. We provide justification for this assertion in Appendix B. This condition is also compatible with results from recent numerical studies in which the interfacial convective flux is about 2 orders of magnitude smaller than the interfacial diffusive flux [*Hidalgo and Carrera*, 2009; *Rongy et al.*, 2012]. As mentioned previously, the top boundary of our porous domain is always saturated with CO$_2$, while the rest is initially free of CO$_2$. We take the pressure p along the top to be 50 bar. (After the onset of convection, there will be small variations in pressure along this layer since the horizontal velocities will be nonzero). For the simulations, we apply periodic conditions along the lateral boundaries of the porous medium. We use periodic boundary conditions because they can be readily implemented numerically, and because we are not interested in surface effects from the sides. Lateral boundary conditions do not play a role in the stability analysis. This is because W and L are taken to be infinitely large so as to allow for perturbations of arbitrarily large wavelengths.

2.4. Fluid and Porous Medium Properties

[11] Table 1 summarizes the fluid and porous medium properties. The temperature is 30°C. The value of α, ρ_0, and ω_{sat} at this temperature and 50 bar is computed using the Cubic-plus-association equation of state described in Appendix A. Using (6) and Table 1, we find $\rho(\omega_{\text{sat}})$ to be 1009.0 kg/m^3, so that $\Delta\rho$ is 11.4 kg/m^3. We use the viscosity of pure water at 30°C and 50 bar reported by the National Institute of Standards and Technology (Chemistry

Table 1. Fluid and Porous Medium Properties

α	ρ_0 (kg/m^3)	ω_{sat} (CO$_2$ mass fraction)	μ (Pa s)	D (m^2/s)	H (m)	W (m)	ϕ (fraction)
0.268	997.6	0.0428	0.0008	2.15×10^{-9}	20	20	0.2

WebBook: Thermophysical properties of fluid systems, http://webbook.nist.gov/chemistry/fluid). The diffusion coefficient is calculated from a correlation built on an irreversible thermodynamics framework [*Mutoru et al.*, 2011]. The height of the medium is 20 m. The width (which affects only the numerical simulations) is also 20 m.

3. Linear Stability Analysis

3.1. Setup

[12] The diffusion-only base state is characterized by the absence of bulk fluid motion ($\tilde{\mathbf{q}}_{base} = \mathbf{0}$), a pressure field $\tilde{P}_{base}$, and a concentration profile $\tilde{\omega}_{base}$ that obeys [*Ennis-King et al.*, 2005; *Xu et al.*, 2006; *Riaz et al.*, 2006; *Slim and Ramakrishan*, 2010]:

$$\frac{\partial \tilde{\omega}_{base}}{\partial \tilde{t}} = \frac{\partial^2 \tilde{\omega}_{base}}{\partial \tilde{z}^2},$$

subject to the conditions

$$\frac{\partial \tilde{\omega}_{base}}{\partial \tilde{z}}\bigg|_{(\tilde{z}=-\mathrm{Ra},\tilde{t})} = 0, \quad \forall \tilde{t},$$

$$\tilde{\omega}_{base}(\tilde{z}=0,\tilde{t}) = 1, \quad \forall \tilde{t},$$

$$\tilde{\omega}_{base}(\tilde{z},0) = 0, \quad -\mathrm{Ra} \leq \tilde{z} < 0.$$

The profile $\tilde{\omega}_{base}$ [*Slim and Ramakrishan*, 2010] is given by

$$\tilde{\omega}_{base}(\tilde{z},\tilde{t}) = 1 + \frac{4}{\pi}\sum_{l=1}^{\infty}\frac{1}{2l-1}\sin\left[\left(l-\frac{1}{2}\right)\frac{\pi\tilde{z}}{\mathrm{Ra}}\right]$$

$$\cdot \exp\left\{-\left[\left(l-\frac{1}{2}\right)\frac{\pi}{\mathrm{Ra}}\right]^2\tilde{t}\right\}. \tag{16}$$

We may express perturbations (denoted with primes) to the base state as

$$\tilde{\mathbf{q}}' = \tilde{\mathbf{q}}, \quad \tilde{P}' = \tilde{P} - \tilde{P}_{base}, \quad \tilde{\omega}' = \tilde{\omega} - \tilde{\omega}_{base}.$$

Substituting these into (8)–(10) and using the form of $\tilde{\omega}_{base}$ in (16) yields

$$\tilde{\mathbf{q}}' = -\nabla\tilde{P}' - \tilde{\omega}'\nabla\tilde{z}, \tag{17}$$

$$\nabla \cdot \tilde{\mathbf{q}}' = 0, \tag{18}$$

$$\frac{\partial \tilde{\omega}'}{\partial \tilde{t}} = -\tilde{w}'\frac{\partial \tilde{\omega}_{base}}{\partial \tilde{z}} - \tilde{\mathbf{q}}' \cdot \nabla\tilde{\omega}' + \gamma\left(\frac{\partial^2 \tilde{\omega}'}{\partial \tilde{x}^2} + \frac{\partial^2 \tilde{\omega}'}{\partial \tilde{y}^2}\right) + \frac{\partial^2 \tilde{\omega}'}{\partial \tilde{z}^2}. \tag{19}$$

The perturbations are assumed to be infinitesimally small, and we may linearize the equations with respect to them by neglecting the second term on the right-hand side of (19) to get

$$\frac{\partial \tilde{\omega}'}{\partial \tilde{t}} = -\tilde{w}'\frac{\partial \tilde{\omega}_{base}}{\partial \tilde{z}} + \gamma\left(\frac{\partial^2 \tilde{\omega}'}{\partial \tilde{x}^2} + \frac{\partial^2 \tilde{\omega}'}{\partial \tilde{y}^2}\right) + \frac{\partial^2 \tilde{\omega}'}{\partial \tilde{z}^2}. \tag{20}$$

Following previous work [*Caltagirone*, 1980; *Ennis-King et al.*, 2005; *Xu et al.*, 2006; *Riaz et al.*, 2006; *Hong and Kim*, 2008; *Rapaka et al.*, 2009; *Slim and Ramakrishan*, 2010], we eliminate $\tilde{P}'$, $\tilde{u}'$, and $\tilde{v}'$ by taking twice the curl of (17), applying (18), and equating the vertical components to obtain

$$\nabla^2\tilde{w}' = -\left(\frac{\partial^2 \tilde{\omega}'}{\partial \tilde{x}^2} + \frac{\partial^2 \tilde{\omega}'}{\partial \tilde{y}^2}\right). \tag{21}$$

The perturbations follow the no-flux and no-flow boundary conditions described in section 2.3:

$$\tilde{w}'(\tilde{x},\tilde{y},\tilde{z}=-\mathrm{Ra},\tilde{t}) = \frac{\partial \tilde{\omega}'}{\partial \tilde{z}}\bigg|_{(\tilde{x},\tilde{y},\tilde{z}=-\mathrm{Ra},\tilde{t})} = 0, \quad \forall \tilde{x},\tilde{y},\tilde{t}, \tag{22}$$

$$\tilde{w}'(\tilde{x},\tilde{y},\tilde{z}=0,\tilde{t}) = \tilde{\omega}'(\tilde{x},\tilde{y},\tilde{z}=0,\tilde{t}) = 0, \quad \forall \tilde{x},\tilde{y},\tilde{t}. \tag{23}$$

Differentiation in the $\tilde{x}\tilde{y}$ plane may be simplified by expressing the perturbations as Fourier transforms in the horizontal directions:

$$\tilde{w}'(\tilde{x},\tilde{y},\tilde{z},\tilde{t}) = \frac{1}{4\pi^2}\int_{-\infty}^{+\infty}\int_{-\infty}^{+\infty}\hat{w}'(\tilde{s}_x,\tilde{s}_y,\tilde{z},\tilde{t})\exp\left[i(\tilde{s}_x\tilde{x}+\tilde{s}_y\tilde{y})\right]d\tilde{s}_x d\tilde{s}_y, \tag{24}$$

$$\tilde{\omega}'(\tilde{x},\tilde{y},\tilde{z},\tilde{t}) = \frac{1}{4\pi^2}\int_{-\infty}^{+\infty}\int_{-\infty}^{+\infty}\hat{\omega}'(\tilde{s}_x,\tilde{s}_y,\tilde{z},\tilde{t})\exp\left[i(\tilde{s}_x\tilde{x}+\tilde{s}_y\tilde{y})\right]d\tilde{s}_x d\tilde{s}_y, \tag{25}$$

where $i = \sqrt{-1}$, and $\tilde{s}_x$, $\tilde{s}_y$ are the dimensionless wave numbers in the $\tilde{x}$ and $\tilde{y}$ directions, respectively. Letting $\tilde{s} = \sqrt{\tilde{s}_x^2 + \tilde{s}_y^2}$ and substituting (24) and (25) into (20) and (21) gives

$$\frac{1}{4\pi^2}\int_{-\infty}^{+\infty}\int_{-\infty}^{+\infty}\left\{\frac{\partial \hat{\omega}'}{\partial \tilde{t}} + \hat{w}'\frac{\partial \tilde{\omega}_{base}}{\partial \tilde{z}} + \gamma\tilde{s}^2\hat{\omega}' - \frac{\partial^2 \hat{\omega}'}{\partial \tilde{z}^2}\right\}$$
$$\cdot \exp\left[i(\tilde{s}_x\tilde{x}+\tilde{s}_y\tilde{y})\right]d\tilde{s}_x d\tilde{s}_y = 0,$$

$$\frac{1}{4\pi^2}\int_{-\infty}^{+\infty}\int_{-\infty}^{+\infty}\left\{\frac{\partial^2 \hat{w}'}{\partial \tilde{z}^2} - \tilde{s}^2\hat{w}' - \tilde{s}^2\hat{\omega}'\right\}\exp\left[i(\tilde{s}_x\tilde{x}+\tilde{s}_y\tilde{y})\right]d\tilde{s}_x d\tilde{s}_y = 0.$$

In order for these relations to hold for all $\tilde{z}$ and $\tilde{t}$, the expressions inside the curly braces must identically be zero. We have then

$$\frac{\partial \hat{\omega}'}{\partial \tilde{t}} = -\hat{w}'\frac{\partial \tilde{\omega}_{base}}{\partial \tilde{z}} + \frac{\partial^2 \hat{\omega}'}{\partial \tilde{z}^2} - \gamma\tilde{s}^2\hat{\omega}', \tag{26}$$

$$\frac{\partial^2 \hat{w}'}{\partial \tilde{z}^2} - \tilde{s}^2\hat{w}' = \tilde{s}^2\hat{\omega}'. \tag{27}$$

The wave numbers $\tilde{s}_x$ and $\tilde{s}_y$ enter the equations only through the combination $\tilde{s}^2 = \tilde{s}_x^2 + \tilde{s}_y^2$. As a result, we may express the

functional form of the transforms as $\hat{w}' = \hat{w}'(\tilde{s}, \tilde{z}, \tilde{t})$ and $\hat{\omega}' = \hat{\omega}'(\tilde{s}, \tilde{z}, \tilde{t})$. The Fourier transforms give a clear physical interpretation of the equations; each mode may be thought of as a wave in the $\tilde{x}\tilde{y}$ plane specified by a wave number $\tilde{s}$ or a wavelength $\tilde{\lambda} = 2\pi/\tilde{s}$. Perturbations are represented as linear superpositions over all possible modes with the wave amplitudes $\hat{w}'$ and $\hat{\omega}'$ acting as weighting factors. Since $\hat{w}'$ and $\hat{\omega}'$ do not depend separately on $\tilde{s}_x$ and $\tilde{s}_y$, the perturbations will be structured symmetrically in the $\tilde{x}\tilde{y}$ plane at least up until the time of onset.

[13] We solve (26) and (27) using the Galerkin method, which has been first applied to this problem by *Ennis-King et al.* [2005] and has been used in several later studies [*Xu et al.*, 2006; *Riaz et al.*, 2006; *Hong and Kim*, 2008; *Rapaka et al.*, 2009; *Slim and Ramakrishan*, 2010]. In this method, we approximate $\hat{w}'$ and $\hat{\omega}'$ by an orthogonal series expansion in $\tilde{z}$, multiply the equations by a complementary set of orthogonal functions, and integrate over $\tilde{z}$ to eliminate the dependence on that variable. This method transforms the coupled partial differential equations (26) and (27) into a system of ordinary differential equations (ODEs). Following past work [*Ennis-King et al.*, 2005; *Xu et al.*, 2006; *Hong and Kim*, 2008; *Rapaka et al.*, 2009; *Slim and Ramakrishan*, 2010], we represent $\hat{w}'$ and $\hat{\omega}'$ by a Fourier series that takes into account the boundary conditions (22) and (23):

$$\hat{w}'(\tilde{s}, \tilde{z}, \tilde{t}) \approx \sum_{n=1}^{N} \hat{w}'_n(\tilde{s}, \tilde{t}) \sin\left(n\pi \frac{\tilde{z}}{\text{Ra}}\right), \tag{28}$$

$$\hat{\omega}'(\tilde{s}, \tilde{z}, \tilde{t}) \approx \sum_{n=1}^{N} \hat{\omega}'_n(\tilde{s}, \tilde{t}) \sin\left[\left(n - \frac{1}{2}\right)\pi \frac{\tilde{z}}{\text{Ra}}\right], \tag{29}$$

where N is sufficiently large to ensure the validity of the approximation. Instead of a Fourier expansion, Riaz et al. use Weber-Hermite functions [*Bell*, 2004]. We discuss more about the differences among the studies in section 3.4. By substituting (28) and (29) into (26) and (27) and applying the Galerkin method, we obtain the ODE system

$$\frac{d\boldsymbol{\omega}_\gamma}{d\tilde{t}} = \mathbf{A}_\gamma \boldsymbol{\omega}_\gamma, \tag{30}$$

where $\boldsymbol{\omega}_\gamma$ is the column vector $(\hat{\omega}'_1, \hat{\omega}'_2, \ldots, \hat{\omega}'_N)^T$, and $\mathbf{A}_\gamma$ is a time-dependent real matrix. This matrix may be represented as $\mathbf{A}_\gamma = \mathbf{B} - \mathbf{CD}^{-1}\mathbf{E}$ with elements

$$B_{mn} = -\left\{\left[\left(n - \frac{1}{2}\right)\frac{\pi}{\text{Ra}}\right]^2 + \gamma\tilde{s}^2\right\}\delta_{mn},$$

$$C_{mn} = \frac{1}{\text{Ra}}\left(\exp\left\{-\left[\left(m + n - \frac{1}{2}\right)\frac{\pi}{\text{Ra}}\right]^2\tilde{t}\right\}\right.$$
$$\left. - \exp\left\{-\left[\left(n - m + \frac{1}{2}\right)\frac{\pi}{\text{Ra}}\right]^2\tilde{t}\right\}\right),$$

$$D_{mn} = \frac{1}{2}\left[\left(\frac{n\pi}{\text{Ra}}\right)^2 + \tilde{s}^2\right]\delta_{mn},$$

$$E_{mn} = \frac{\tilde{s}^2}{\pi}(-1)^{m+n}\frac{4m}{4m^2 - (2n-1)^2},$$

where δ_{mn} is the Kronecker delta and $\{(m,n) \in \mathbb{N} : (m,n) \le N\}$. A derivation of (30) is presented in Appendix C. We determine the critical time t_c using the criterion introduced by Slim and Ramakrishnan. At each time $\tilde{t}$, we compute a functional σ that represents the maximum normalized instantaneous growth rate of the wave amplitudes:

$$\sigma(\tilde{t}) = \sup_{\tilde{\omega}'}\left[\frac{d}{d\tilde{t}}\left(\int \tilde{\omega}'^2 d\tilde{V}\right)\bigg/\left(\int \tilde{\omega}'^2 d\tilde{V}\right)\right]. \tag{31}$$

Here, $d\tilde{V} = d\tilde{x}d\tilde{y}d\tilde{z}$ and the integration is carried out over the entire porous domain. In terms of the Fourier transforms, σ is

$$\sigma(\tilde{t}) = \sup_{\hat{\omega}'}\left[\frac{d}{d\tilde{t}}\left(\int_{-\text{Ra}}^0 |\hat{\omega}'|^2 d\tilde{z}\right)\bigg/\left(\int_{-\text{Ra}}^0 |\hat{\omega}'|^2 d\tilde{z}\right)\right], \tag{32}$$

where it is to be maximized over all Fourier modes. Using the form of $\hat{\omega}'$ in (29), σ may be approximated as

$$\sigma \approx \sup_{\boldsymbol{\omega}_\gamma}\frac{\frac{d}{d\tilde{t}}\left(\boldsymbol{\omega}_\gamma^\dagger \boldsymbol{\omega}_\gamma\right)}{\boldsymbol{\omega}_\gamma^\dagger \boldsymbol{\omega}_\gamma} = \sup_{\boldsymbol{\omega}_\gamma}\frac{\boldsymbol{\omega}_\gamma^\dagger\left(\mathbf{A}_\gamma + \mathbf{A}_\gamma^T\right)\boldsymbol{\omega}_\gamma}{\boldsymbol{\omega}_\gamma^\dagger \boldsymbol{\omega}_\gamma}, \tag{33}$$

where $\dagger$ indicates the conjugate transpose. Since $\mathbf{A}_\gamma + \mathbf{A}_\gamma^T$ is a real symmetric matrix, it has real eigenvalues and is diagonalizable. Thus, we may express $\boldsymbol{\omega}_\gamma$ in terms of the eigenvectors of $\mathbf{A}_\gamma + \mathbf{A}_\gamma^T$, so that the rightmost expression of (33) is equal to its most positive eigenvalue. That is,

$$\sigma \approx \sup_i \Lambda_i, \tag{34}$$

where Λ_i are the eigenvalues of $\mathbf{A}_\gamma + \mathbf{A}_\gamma^T$. We define the critical time t_c to be the earliest instance when a Fourier mode begins to grow ($\sigma > 0$). The critical wavelength λ_c is determined by this earliest-growing mode. The advantages of this criterion for t_c over other criteria is that we do not need to use an arbitrary initial condition for $\boldsymbol{\omega}_\gamma$, nor is it necessary to integrate the ODE system (30) [*Slim and Ramakrishan*, 2010]. To find t_c, we compute the eigenvalues of $\mathbf{A}_\gamma + \mathbf{A}_\gamma^T$ for many points in the space of possible values for $\tilde{s}$ and $\tilde{t}$.

[14] One can also perform a nonlinear stability analysis in which the amplitude of the perturbations may be arbitrarily large. In this case, the second term on the right-hand side of (19) cannot be neglected. The method proceeds by substituting (19) into the form of σ in (31) and maximizing that functional subject to the constraints (17) and (18). Doing this yields a set of Euler-Lagrange equations that may be solved to obtain the critical time and critical wavelength. The nonlinear term can be expressed as $-\tilde{\mathbf{q}}' \cdot \nabla\tilde{\omega}' = -\nabla \cdot (\tilde{\omega}'\tilde{\mathbf{q}}')$ because of (18). Using the divergence theorem, its contribution to (31) may be converted to a surface integral. This surface integral can be nonzero only along the lateral sides. *Slim and Ramakrishnan* [2010] reason that in the limit of an infinitely large domain, it is negligible compared to the denominator of (31). (The surface integral would still vanish in a finite-sized domain because one normally uses periodic boundary conditions or no-flux conditions along the lateral walls in such a case). This reasoning holds for both isotropic and anisotropic media. Thus, the nonlinear term does not add to the instability of the base state, and both types of stability analyses will produce the same results.
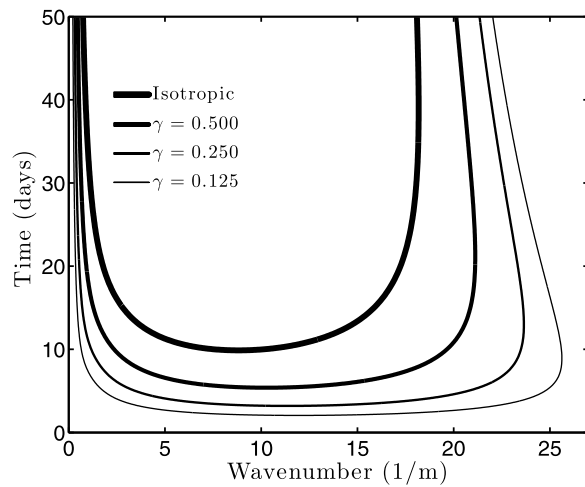
Figure 1. Contours of $\sigma = 0$ in wave number–time space around t_c for a fixed vertical permeability of $k_z = 0.500$ darcy (Ra ≈ 3200). The scales on the axes would change for a different k_z (Ra), but the figure would be otherwise identical. As explained in the text, the contours are loops which become closed at times much later than those shown here. The diffusion-only base state is unstable ($\sigma > 0$) within each loop and stable outside of each loop so that the contours represent states of marginal stability.

3.2. Analytical Results

[15] As mentioned in section 1, we are interested in the effect of permeability anisotropy on the critical time t_c and critical wavelength λ_c when the vertical permeability k_z is fixed. The horizontal permeability k_h is greater than k_z ($\gamma < 1$) in natural permeable formations. The increased k_h allows perturbations to propagate more easily through the medium, thereby enhancing the rate of mixing. We therefore expect anisotropy to reduce t_c. We present analytical arguments to show that this is indeed true. In this section, we use the subscript γ to denote quantities that apply to anisotropic media, and we use the subscript iso for quantities that apply to isotropic media. An examination of (30) reveals that

$$\mathbf{A}_\gamma = \mathbf{A}_{\mathrm{iso}} - \tilde{s}^2(\gamma - 1)\mathbf{I}, \qquad (35)$$

where $\mathbf{I}$ is the identity matrix. From (34), we see that

$$\sigma_\gamma = \sigma_{\mathrm{iso}} - 2\tilde{s}^2(\gamma - 1). \qquad (36)$$

Since $\gamma < 1$, we have $\sigma_\gamma > \sigma_{\mathrm{iso}}$. Equation (36) therefore shows that anisotropy makes all modes more unstable than they would be in isotropic media; it always decreases the critical time. Moreover, the difference between σ_γ and σ_{iso} becomes larger with $\tilde{s}$ because the increased instability is biased toward modes with larger dimensionless wave numbers $\tilde{s}$. That is, anisotropy reduces the dimensionless critical wavelength $\tilde{\lambda}_c$. It is not apparent from this equation, however, if the actual, physical wavelength λ_c will decrease with increasing anisotropy, because λ_c scales inversely with the square root of γ according to $\lambda_c = \ell\tilde{\lambda}_c/\gamma^{1/2}$. We show in the following sections that λ_c does decrease with increasing anisotropy.

[16] We also have

$$\boldsymbol{\omega}_\gamma = \exp\left[-\tilde{s}^2(\gamma - 1)\tilde{t}\right]\boldsymbol{\omega}_{\mathrm{iso}}. \qquad (37)$$

We can derive (37) by substituting (35) into (30) and multiplying both sides by the integrating factor $\exp\left[\tilde{s}^2(\gamma - 1)\tilde{t}\right]$ to get

$$\frac{d\mathbf{r}}{d\tilde{t}} = \mathbf{A}_{\mathrm{iso}}\mathbf{r},$$

where $\mathbf{r} = \exp\left[\tilde{s}^2(\gamma - 1)\tilde{t}\right]\boldsymbol{\omega}_\gamma$. At $\tilde{t} = 0$, the exponential term becomes unity. The vectors $\boldsymbol{\omega}_\gamma$ and $\boldsymbol{\omega}_{\mathrm{iso}}$ are identical at this time because mixing occurs only when $\tilde{t} > 0$ so that anisotropy has no effect at $\tilde{t} = 0$. Therefore, $\mathbf{r}$ obeys the same ODE system as $\boldsymbol{\omega}_{\mathrm{iso}}$ and is described by the same initial condition. We can thus equate the two vectors, which leads to (37). Note that we can obtain (36) if we substitute (35) and (37) into (33). Anisotropy amplifies the perturbations via an exponential factor that grows in time, with larger growth rates for modes with larger $\tilde{s}$. The end result is that it reduces t_c and λ_c.

3.3. Contours in Wave Number–Time Space

[17] Figure 1, which is a key element of our work, shows contours of $\sigma = 0$ for a fixed vertical permeability of $k_z = 0.500$ darcy (Ra ≈ 3200). Figure 1 would appear the same for other values of k_z (Ra), except that the scales on the abscissa and the ordinate would be different. The contours are loops which become closed at times much later than those shown in the figure. We focus on early times in order to more clearly see the effect of anisotropy on t_c and λ_c. The contours represent states of marginal stability; the diffusion-only base state is unstable ($\sigma > 0$) within each loop and stable outside of each loop. Before the onset time, the unstable dense fluid layer is insufficiently thick for the perturbation modes to grow before being stabilized by diffusion. As a result, they decay in amplitude during this initial period. Dissipation by diffusion is also why onset may occur for only an intermediate range of wave numbers. For instance, large wave number (short wavelength) modes generate relatively strong perturbations, but act over only short distances. Small wave number (long wavelength) modes hardly perturb the system at all because they are stretched over long distances. In both cases, diffusion is able to overwhelm the perturbations. The base state becomes stable again at very long times when the porous domain gets close to saturation, and the fluids become quiescent.

[18] The critical time and critical wavelength may be estimated from Figure 1. For each anisotropy ratio, t_c is given by the minimum of the corresponding contour. The mode associated with t_c is characterized by λ_c. We showed in the previous section that anisotropy makes all modes more unstable. This reduces t_c and widens the contours. The increased instability is more prominent for larger wave number modes, which leads to a reduction in λ_c. The figure also shows that the contours become more flattened around t_c as γ decreases. This indicates that anisotropy increases the parity among the modes, making more of them almost equally unstable with the earliest-growing mode. In other words, the notion of a critical wavelength becomes less meaningful with increasing anisotropy.
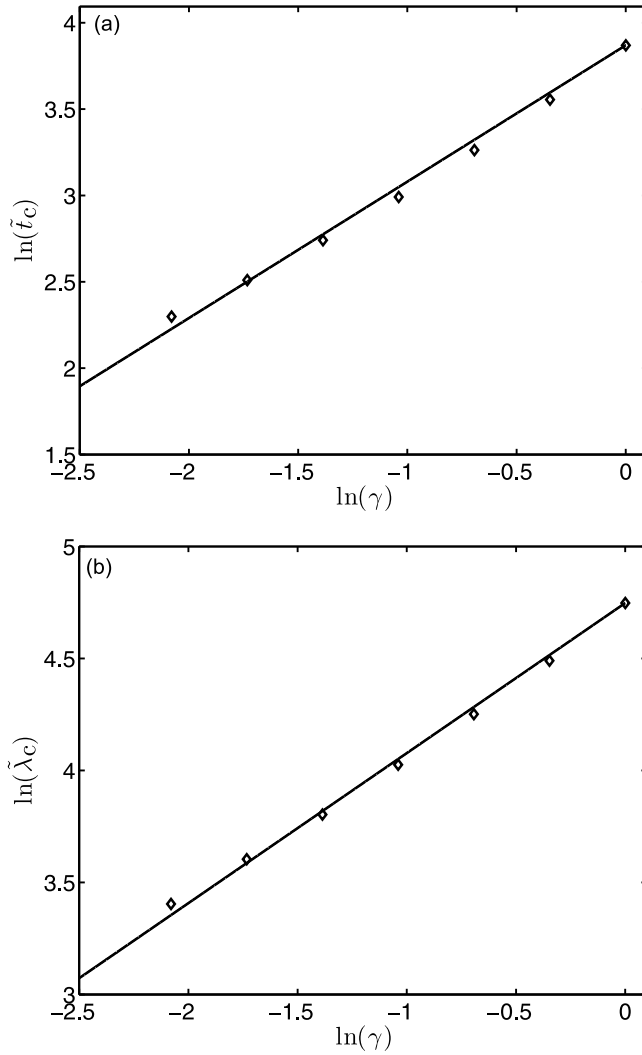
Figure 2. (a) Dimensionless critical time $\tilde{t}_c$ versus the anisotropy ratio γ on a log-log plot. The slope and intercept of the regression line are 0.79 and 3.87, respectively. (b) Dimensionless critical wavelength $\tilde{\lambda}_c$ versus γ on a log-log plot. The slope and intercept of the regression line are about 0.67 and 4.75, respectively.

3.4. Scaling Relations for the Critical Time and the Critical Wavelength

[19] From the choice of nondimensionalizations in section 2.2, the critical time in isotropic media must scale with fluid and porous medium properties according to $t_c \sim \tau = D(\phi\mu/k\Delta\rho g)^2$, where $k = k_z = k_h$. The critical wavelength scales as $\lambda_c \sim \ell = D\phi\mu/k\Delta\rho g$. We find $\tilde{t}_c$ to be 47.9 and $\tilde{\lambda}_c$ to be 115.3. Thus, in isotropic media we have

$$t_c = 47.9 D \left(\frac{\phi\mu}{k\Delta\rho g} \right)^2, \tag{38}$$

$$\lambda_c = 115.3 D \frac{\phi\mu}{k\Delta\rho g}. \tag{39}$$

Equation (38) exactly reproduces the result by *Slim and Ramakrishnan* [2010]. They find the t_c given by (38) to be one to two times smaller than the t_c computed using methods from some past studies [*Lick*, 1965; *Ennis-King et al.*, 2005; *Xu et al.*, 2006] and several times smaller than the prediction by *Riaz et al.* [2006]. The reason for the large discrepancy between that study and the other studies is because Riaz et al. define the critical time differently. They use an orthogonal (Weber-Hermite function) expansion for $\hat{w}'$ and $\hat{\omega}'$ that is truncated after only the first-order term. This term represents the slowest-decaying mode during the initial period, which they call the "dominant mode" [*Riaz et al.*, 2006]. They define the critical time as the first instance when this mode begins to grow. All other studies, including this work, define the critical time by the earliest-growing mode.

[20] Figure 2 shows the dependence of the dimensionless critical time and the dimensionless critical wavelength on γ. The slope and intercept of the regression line in Figure 2a are 0.79 and 3.87, respectively. Thus, the actual critical time for a fixed k_z is

$$t_c = 47.9\gamma^{0.79} D \left(\frac{\phi\mu}{k_z\Delta\rho g} \right)^2. \tag{40}$$

This equation shows the strong influence of the vertical permeability on the critical time. As expected, k_z has a greater effect on t_c than does k_h. This suggests that the growth of the perturbations is rate limited by the vertical velocity $\tilde{w}'$, which depends on k_z and which determines their ability to travel vertically through the medium and disturb the unstable density gradient. We discuss in section 4.3 how (21) implies an upper bound on $\tilde{w}'$, and thus also a lower bound on t_c for a given γ and set of parameters. Even though the relative reduction in t_c due to anisotropy is the same regardless of the value of k_z, the absolute reduction is greater when k_z is low. For example, at $k_z = 0.125$ darcy, t_c is 158 days for isotropic media and 31 days for $\gamma = 0.125$. The same comparison at $k_z = 1.000$ darcy gives 2.47 days for isotropic media and 0.48 days for $\gamma = 0.125$. One interpretation is that, in absolute terms, the enhanced mixing from the increased k_h is more pronounced when k_z is low and t_c is large. This may have some practical implications: low k_z anisotropic formations might still be attractive for site selection purposes as long as k_z is not too low and k_h is sufficiently high. The slope and intercept of the regression line in Figure 2b are about 0.67 and 4.75, respectively. Since the actual wavelength scales according to $\lambda_c = \ell\tilde{\lambda}_c/\gamma^{1/2}$, we find

$$\lambda_c = 115.3\gamma^{0.17} D \frac{\phi\mu}{k_z\Delta\rho g}. \tag{41}$$

We must be cautious when applying (41), because we have seen that λ_c becomes less meaningful with increasing anisotropy as more modes become nearly equally unstable with the earliest-growing mode.

[21] *Xu et al.* [2006] have previously studied the effect of anisotropy when k_z is fixed (see section 1). They determine t_c using a quantity that is essentially identical to σ. The main difference is that their approach involves integrating (30) over time instead of evaluating the eigenvalues of $\mathbf{A}_\gamma + \mathbf{A}_\gamma^T$. They use a "white noise" initial condition $[\hat{\omega}_1'(\tilde{s}, \tilde{t}=0), \hat{\omega}_2'(\tilde{s}, \tilde{t}=0), \ldots, \hat{\omega}_N'(\tilde{s}, \tilde{t}=0)]^T = (1, 1, \ldots, 1)^T \forall \tilde{s}$, which has been found to permit faster growth rates than some other initial conditions for a related problem in open space (nonporous media) [*Foster*, 1965]. Their results are:

Table 2. Ratio of Critical Times ($t^* = 0.64\gamma^{-0.16}$) and Critical Wavelengths ($\lambda^* = 1.20\gamma^{0.02}$) From This Study With Results From *Xu et al.* [2006]

γ	t^*	λ^*
Isotropic	0.64	1.20
0.500	0.72	1.18
0.250	0.80	1.17
0.125	0.89	1.15

$t_c = 75.2\gamma^{0.95}D(\phi\mu/k_z\Delta\rho g)^2$ and $\lambda_c = 96.2\gamma^{0.15}D\phi\mu/k_z\Delta\rho g$. We may compare these equations to (40) and (41) by defining the ratios $t^* = 47.9\gamma^{0.79}/75.2\gamma^{0.95} = 0.64\gamma^{-0.16}$ and $\lambda^* = 115.3\gamma^{0.17}/96.2\gamma^{0.15} = 1.20\gamma^{0.02}$. Our results for t_c and λ_c are similar to those predicted by Xu *et al.* for the range of γ considered (Table 2), as we expect.

4. Numerical Simulations

4.1. Overview

[22] For completeness we present an overview of the numerical scheme; details may be found in earlier references [*Tan and Homsy*, 1988; *Bestehorn*, 1993; *Thess and Orszag*, 1995; *Bestehorn and Colinet*, 2000]. We have performed simulations at four different vertical permeabilities: $k_z = 0.125$ darcy (Ra ≈ 800), $k_z = 0.250$ darcy (Ra ≈ 1600), $k_z = 0.500$ darcy (Ra ≈ 3200), and $k_z = 1.000$ darcy (Ra ≈ 6400). For each k_z, we have simulated isotropic media and anisotropic media with $\gamma = 0.500$, $\gamma = 0.250$, and $\gamma = 0.125$. Most of the results we present are for Ra ≈ 3200.

[23] The equations are discretized on a uniform mesh using finite differences, with N_x, N_z grid points in the $\tilde{x}$ and $\tilde{z}$ directions, respectively. Table 3 lists the number of grid points in our simulations. The CO₂ concentration gradient associated with the average diffusive flux at $\tilde{z} = 0$, which we denote as J_d, strongly influences the behavior that we observe because J_d determines the CO₂ dissolution rate. We use fine enough gridding to faithfully capture the gradient. Since the dimensions of our porous medium are 20 m × 20 m, the grid spacing in our simulations is less than 1 cm. We are able to achieve grid convergence if the coarser grid simulations are limited to the same maximum time step size $\Delta\tilde{t}$ as the fine grid simulation. Figure 3 compares the growth of the average saturation $\langle\tilde{\omega}\rangle$ with time for different grid resolutions at Ra ≈ 3200. The average saturation is defined as the spatially averaged value of $\tilde{\omega}$ expressed as a percentage. The figure shows good overlap of the curves for both isotropic media and for the smallest anisotropy ratio we have simulated ($\gamma = 0.125$). We discuss more about dissolution rates in section 4.2.

[24] The problem is initialized by setting $\tilde{\omega}$ equal to zero everywhere, except along the top layer where we introduce perturbations such that

$$\tilde{\omega}\left(\tilde{x}_i, \tilde{z}_j = 0, \tilde{t}^0\right) = \tilde{\omega}_{i,1}^0 = 1 + \xi_i^0, \quad \forall i,$$

Table 3. Number of Grid Points Used in the Simulations

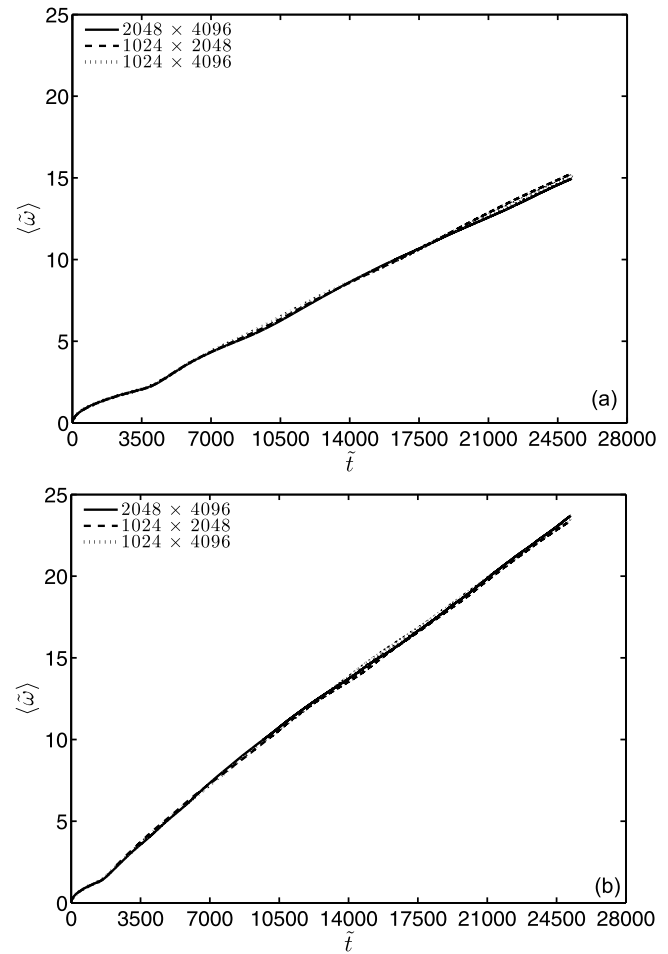| Simulation	N_x	N_z
Ra ≈ 800, $\forall\gamma$	2048	2048
Ra ≈ 1600, $\forall\gamma$	2048	2048
Ra ≈ 3200, $\forall\gamma$	2048	4096
Ra ≈ 6400, $\forall\gamma$	4096	4096

Figure 3. Increase in the average saturation $\langle\tilde{\omega}\rangle$ with the dimensionless time for different grid resolutions: (a) Isotropic media and (b) anisotropic media with $\gamma = 0.125$ (Ra ≈ 3200).

with ξ_i^0 being a randomly generated set of numbers between -0.00125 and 0.00125. All indices henceforth will be implied to run through their entire allowable range, except when otherwise noted. We use time-varying perturbations where a different random set of numbers ξ_i^n is generated at each time $\tilde{t}^n$, but the maximum amplitude of the perturbations remains fixed. This choice of perturbing the system is simple to implement and has also been used in past studies [*Riaz et al.*, 2006; *Xie et al.*, 2011; *Elenius and Johannsen*, 2012]. The observed dynamics depend to some degree on how the system is numerically perturbed (see Elenius and Johannsen for a detailed statistical analysis), but careful use of sensitivity studies can limit this dependence. The amplitude of the perturbations must not be so large as to introduce unphysical disturbances, yet not so small that they are dissipated by diffusion and onset of convection does not occur. Our tests show that increasing or decreasing the maximum amplitude by a factor of four does not significantly affect $\langle\tilde{\omega}\rangle$. The diffusive flux J_d undergoes fluctuations after some time [*Crank*, 1980], and using different random number seeds can noticeably affect the fluctuation patterns and the convective fingering patterns [*Pau et al.*, 2010; *Elenius and Johannsen*, 2012]. However, the differences in $\langle\tilde{\omega}\rangle$ are small (comparable to those in Figure 3) over the entire
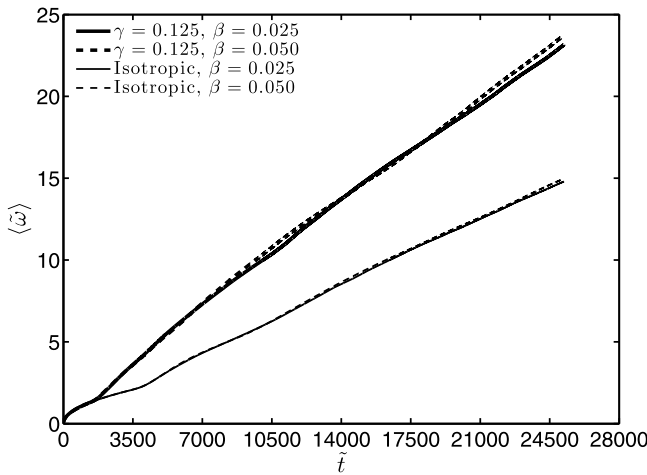
Figure 4. Sensitivity of the average saturation $\langle \tilde{\omega} \rangle$ to β (used in equation (42)) in isotropic media and in anisotropic media with $\gamma = 0.125$ (Ra ≈ 3200).

duration of our simulations. Since $\langle \tilde{\omega} \rangle$ is proportional to the time integral of J_d [*Doering and Constantin*, 1998; *Hassanzadeh et al.*, 2007; *Slim and Ramakrishan*, 2010], we can conclude that the time-averaged mean dissolution rate is rather robust. These findings agree with the results from Pau et al. We have observed that trends in the maximum Darcy velocities $\tilde{u}_{\max}$ and $\tilde{w}_{\max}$, where we define $\tilde{u}_{\max} = \sup\left\{ \left| \tilde{u}_{i,j}^n \right| : \forall i, j \right\}$ and apply a similar definition for $\tilde{w}_{\max}$, can be reliably reproduced with different random number seeds.

[25] We outline in the rest of this section the main computations taken in each time step. The value of $\tilde{\omega}$, and hence the right-hand side of (14), is known everywhere at the beginning of a time step, either from the initial condition or having been computed from the previous time step. We solve for ψ via a pseudospectral method that involves applying discrete Fourier transforms in the horizontal direction and finite differences in the vertical direction, leading to a tridiagonal system that is to be solved. Our method is similar to those described in previous papers [*Tan and Homsy*, 1988; *Bestehorn*, 1993; *Thess and Orszag*, 1995; *Bestehorn and Colinet*, 2000]. The Poisson's equation solver routine at each time step performs N_z forward transforms, follows that with N_x tridiagonal solves, and finishes with N_z inverse transforms. It employs fast Fourier transform routines from the Fortran package FFTPACK [*Swarztrauber*, 1982], and it solves the tridiagonal systems using the Thomas algorithm. We calculate the velocities $\tilde{u}_{i,j}^n$ and $\tilde{w}_{i,j}^n$ at each grid point from (12) and (13). Convective fluxes are computed at the cell faces using the donor cell method [*Roache*, 1998], which is a type of upwinding scheme.

[26] The left-hand side and the diffusion term in (15) are discretized according to an explicit forward time, centered space scheme. The resulting equation can be easily rearranged to obtain an expression for $\tilde{\omega}_{i,j}^{n+1}$ in terms of known quantities. The dimensionless step size $\Delta \tilde{t}$ is updated every ten time steps according to

$$\Delta \tilde{t} = \inf\left\{ \beta\left((\Delta \tilde{x})^2, (\Delta \tilde{z})^2, \frac{\phi \Delta \tilde{x}}{\tilde{u}_{\max}}, \frac{\phi \Delta \tilde{z}}{\tilde{w}_{\max}} \right) \right\}, \qquad (42)$$

Table 4. Values of β Used to Compute the Time Step Size $\Delta \tilde{t}$ in Equation (42)

Simulation	β
Ra ≈ 800, isotropic, and $\gamma = 0.500$	0.050
Ra ≈ 800, $\gamma = 0.250$, and $\gamma = 0.125$	0.100
Ra ≈ 1600, $\forall \gamma$	0.025
Ra ≈ 3200, $\forall \gamma$	0.025
Ra ≈ 6400, $\forall \gamma$	0.050

The third and fourth constraints come from the Courant-Friedrichs-Lewy (CFL) condition. The first two come from a diffusion-determined limit; they (especially the first one in anisotropic media) are usually more restrictive than the limits set by CFL condition. For the simulations at Ra ≈ 3200, we use $\beta = 0.025$. Figure 4 shows that doubling the time step size so that $\beta = 0.050$ does not have much effect on the results. Table 4 summarizes the values of β used in our simulations. We use larger values of β in some cases so that the results we present in this paper can be attained within a practical amount of wall time. We note that in the simulations where $\beta = 0.100$, the dimensionalized time step Δt is always less than 20 min, while the total simulation time extends for nearly 150 years. The step size is constrained so that it cannot increase by more than 5% between each update. We apply periodic boundary conditions through the lateral boundaries, no-flow conditions through the top boundary, and no-flux conditions through the bottom boundary. The value of $\tilde{\omega}$ along the top layer is "updated" by generating a new set of random numbers ξ_i^n, as described earlier. The program terminates when some user-specified time is reached.

4.2. Dissolution Rates

[27] Figure 5 shows the evolution of the average saturation $\langle \tilde{\omega} \rangle$ with time. It is connected with the dimensionless average vertical diffusive flux along the top layer $\tilde{J}_d$, which is presented in Figure 6. This important quantity determines
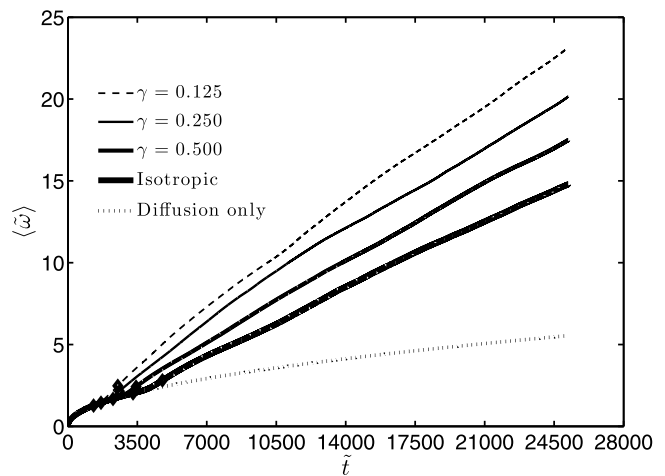

Figure 5. Increase over time in the average saturation $\langle \tilde{\omega} \rangle$, where diamonds indicate inflection points. The inflection points occur earlier with increasing anisotropy. Compared to the isotropic case, a mildly anisotropic ($\gamma = 0.125$) medium is able to dissolve over 50% more CO$_2$ by the end of our simulations (Ra ≈ 3200).
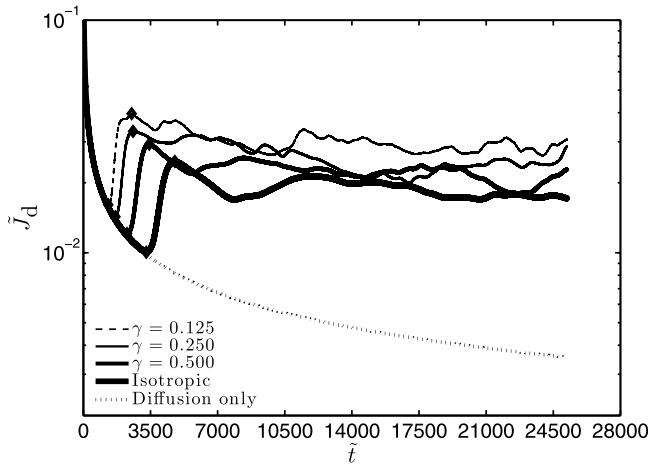
Figure 6. Temporal evolution of the dimensionless average vertical diffusive flux along the top layer $\tilde{J}_d$, where diamonds indicate local extrema. This flux represents the dissolution rate of CO$_2$ into the porous domain and is generally higher in more anisotropic media. The time-averaged mean dissolution rate, which is proportional to $\langle\tilde{\omega}\rangle$, becomes larger with increasing anisotropy (Ra $\approx$ 3200).

the dissolution rate of CO$_2$ into the porous domain. We define it as

$$\tilde{J}_d = \frac{1}{\tilde{W}}\int_0^{\tilde{W}}\frac{\partial\tilde{\omega}}{\partial\tilde{z}}\bigg|_{\tilde{z}=0}d\tilde{x}, \tag{43}$$

where $\tilde{W} = W\gamma^{1/2}/\ell$. The gradient in (43) is approximated numerically by finite differences between the top two rows of grid points. By integrating (5) over space, using the divergence theorem, and applying the periodic boundary conditions, we can show that $\langle\tilde{\omega}\rangle$ is proportional to the time integral of $\tilde{J}_d$ [*Doering and Constantin*, 1998; *Hassanzadeh et al.*, 2007; *Slim and Ramakrishan*, 2010] so that an inflection point of $\langle\tilde{\omega}\rangle$ corresponds to a local extremum of $\tilde{J}_d$.

[28] Initially, CO$_2$ is transported by diffusion only. During this period, $\tilde{\omega}$ obeys the concentration profile (16). For ease of computation, we approximate this profile by an error function. Transport by diffusion is sufficiently slow that the bottom of the porous domain appears to be far away even after long times. As a result, we can take the boundary condition at the bottom to be $\tilde{\omega}(\tilde{z}\to-\infty)=0$, and (16) may be approximated as

$$\tilde{\omega}_{\text{diffusion}}(\tilde{z},\tilde{t}) = 1 + \text{erf}\left(\frac{\tilde{z}}{2\sqrt{\tilde{t}}}\right), \tag{44}$$

where erf(x) is the error function [*Carslaw and Jaeger*, 1986]. The dotted line in Figure 6 is produced by substituting (44) into (43), which yields

$$\tilde{J}_{d,\text{diffusion}} = \frac{1}{\sqrt{\pi\tilde{t}}}. \tag{45}$$

When transport initially occurs only by diffusion, $\tilde{J}_d$ decreases with the square root of time according to (45), while $\langle\tilde{\omega}\rangle$ increases with the square root of time. Eventually there is onset of convection and $\tilde{\omega}$ begins to evolve away from the one-dimensional profile in (44).

[29] At some time after onset of convection, the dissolution rate $\tilde{J}_d$ reaches a local minimum and $\langle\tilde{\omega}\rangle$ experiences an inflection point. Convection starts to significantly affect transport rates around this $\tilde{t}_{\min}$. It represents a state when diffusion, which generally brings CO$_2$ from the top layer to the layer slightly below it, is balanced by the local convective flux along the lower layer, which generally takes CO$_2$ away from that layer. For all anisotropy ratios, there is large difference between $\tilde{t}_c$ and $\tilde{t}_{\min}$. Figures 5 and 6 show that $\tilde{t}_{\min}$ is 1 to 2 orders of magnitude larger than $\tilde{t}_c$ (which equals 47.9). Previous numerical simulations in isotropic media [*Hassanzadeh et al.*, 2007; *Pruess and Zhang*, 2008; *Pau et al.*, 2010; *Elenius and Johannsen*, 2012] and experiments in Hele-Shaw cells [*Kneafsey and Pruess*, 2010] have also observed the same order of magnitude difference. The increased horizontal permeability k_h from anisotropy allows instabilities to propagate more easily through the medium as they grow in time. This leads to a significant reduction in the gap between $\tilde{t}_c$ and $\tilde{t}_{\min}$. It is reflected in the earlier and more dramatic rise in $\langle\tilde{\omega}\rangle$ for smaller γ.

[30] There is a period after $\tilde{t}_{\min}$ during which the local convective flux overwhelms $\tilde{J}_d$ so that the magnitude of the gradient $\partial\tilde{\omega}/\partial\tilde{z}$ at $\tilde{z}=0$, and thus also $\tilde{J}_d$, increases. The dissolution rate increases until it reaches a local maximum, where it again becomes balanced by the convective flux. This $\tilde{t}_{\max}$ is another inflection point of $\langle\tilde{\omega}\rangle$. Since convection becomes stronger with increasing anisotropy, it must be balanced by a higher $\tilde{J}_d$ at this time. The dissolution rate after $\tilde{t}_{\max}$ is also generally greater in more anisotropic media. This is because more intensive convective flows permit larger concentration gradients at $\tilde{z}=0$ to be sustained for longer periods of time. The fluctuations in $\tilde{J}_d$ after $\tilde{t}_{\max}$ are caused by the continual interplay between it and the local convective flux [*Crank*, 1980]. These fluctuations have also been observed in past studies [*Pruess and Zhang*, 2008; *Pau et al.*, 2010; *Elenius and Johannsen*, 2012]. A more robust quantity is the time-averaged mean dissolution rate, which is proportional to $\langle\tilde{\omega}\rangle$ and which clearly becomes larger with increasing anisotropy. Compared to the isotropic case, a mildly anisotropic ($\gamma = 0.125$) medium is able to dissolve
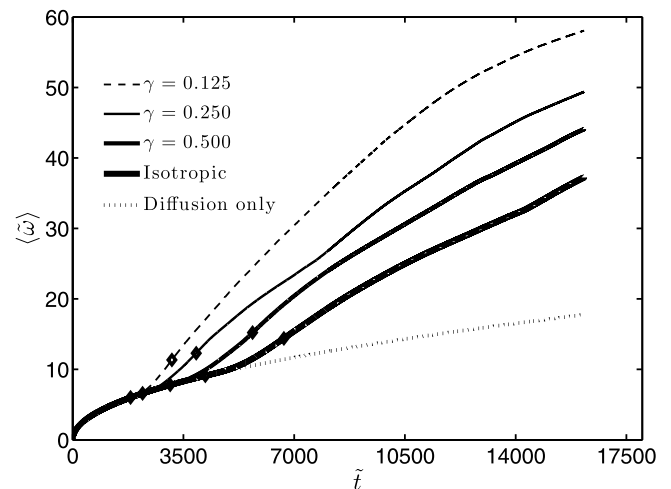

Figure 7. Increase over time in $\langle\tilde{\omega}\rangle$ at a lower Rayleigh number of Ra $\approx$ 800. Anisotropy continues to have an effect even as $\langle\tilde{\omega}\rangle$ begins to plateau.
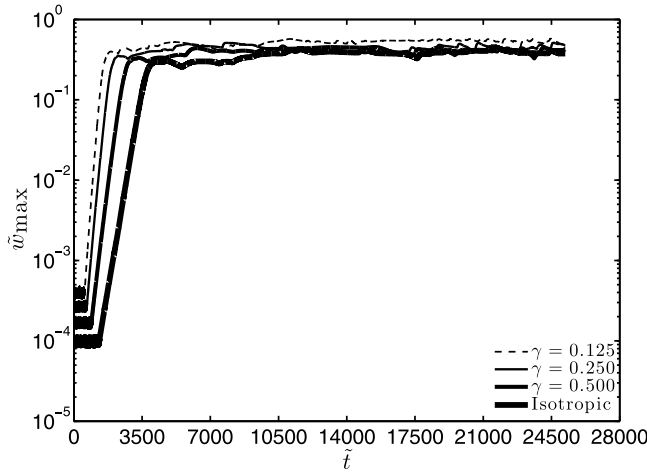
Figure 8. Temporal evolution of the maximum vertical Darcy velocity $\tilde{w}_{\max}$. The increased k_h from anisotropy allows fluid velocities to develop more rapidly and intensifies the convection (Ra ≈ 3200).

over 50% more CO_2 by the end of our simulations. At times later than those in Figures 5 and 6, $\langle \tilde{\omega} \rangle$ will eventually flatten out, and $\tilde{J}_d$ will decrease to zero as the porous medium becomes saturated with CO_2. This is demonstrated in Figure 7 for the case of Ra ≈ 800, which corresponds to a domain with a smaller dimensionless height. Note that anisotropy continues to have an effect even as $\langle \tilde{\omega} \rangle$ begins to plateau.

4.3. Velocities

[31] Figure 8 shows the change in the maximum vertical Darcy velocity $\tilde{w}_{\max}$ over time. Because of the numerical perturbations, $\tilde{w}_{\max}$ experiences fluctuations around a small mean value. At some point, the fluids become sufficiently unstable for $\tilde{w}_{\max}$ to undergo a rapid growth. For all γ, this time is earlier than the corresponding $\tilde{t}_{\min}$. This is because the velocities must develop to a certain extent before convection is able to significantly affect the CO_2 dissolution rate. Anisotropy allows velocities to develop more rapidly and strengthens the intensity of the convection. The velocities continue to rise until around $\tilde{t}_{\max}$, after which $\tilde{w}_{\max}$ fluctuates about a mean maximum value.

[32] We suggested in section 3.4 that there exists an upper limit on the perturbation velocity $\tilde{w}'$. This may be related to fact that $\tilde{w}_{\max}$ (which is computed from ψ) is limited to a mean maximum value. Comparing (21) and (14), we see that both involve a Poisson's equation in which the Laplacian of a scalar velocity measure ($\tilde{w}'$ or ψ) is equated to horizontal gradients of the CO_2 concentration field in the domain. The Laplacian of $\tilde{w}'$ (or ψ) at an arbitrary point $\tilde{x}$ is proportional to the difference between an average value of $\tilde{w}'$ (ψ) around $\tilde{x}$ and the value of $\tilde{w}'$ (ψ) at $\tilde{x}$. (This is clear if one considers the standard finite difference discretization of the Laplace operator). Transport processes, both diffusion and convection, tend to minimize gradients of the concentration field so that the right hand sides of (21) and (14) are bounded in magnitude. As a result, the difference between the value of $\tilde{w}'$ (ψ) at $\tilde{x}$ and an average value around $\tilde{x}$ is also bounded. This means that there is a limit on the maximum velocities that may develop within the medium.

[33] Adopting an idea introduced in an earlier work [*Xie et al.*, 2011], we have recorded the location of the deepest front (DF; Figure 9). For clarity we present the distance along the z coordinate in dimensional terms ($\tilde{z}$ ranges from $\tilde{z} = 0$ to $\tilde{z} = -$Ra ≈ -3200). We define the DF as the deepest point where $\tilde{\omega}$ is greater than 0.001 (i.e., where ω greater is 0.1% of ω_{sat}). Its rate of change in time gives an indication of the maximum fingering velocities. The DF when there is only diffusion is computed from (44). Convection substantially accelerates the change in the DF after enough time has elapsed. Anisotropy generally leads to larger fingering velocities, especially during the earlier stages of mixing. The trend in the DF at later times becomes more unpredictable because of nonlinear processes (particularly finger splitting) discussed in section 4.4. Nevertheless, it reaches the bottom earlier in the two most anisotropic cases than it does in the isotropic case.

4.4. Concentration Profiles

[34] Snapshots of the CO_2 concentration field at Ra ≈ 3200 in isotropic media and for $\gamma = 0.125$ are illustrated in Figures 10 and 11, respectively. For clarity we present the distance along the x and z coordinates in dimensional terms. In Figure 10, $\tilde{x}$ ranges up to $\tilde{x} = $ Ra ≈ 3200, while it ranges up to $\tilde{x} = $ Ra$(0.125)^{1/2} \approx 1100$ in Figure 11. In both figures, $\tilde{z}$ ranges from $\tilde{z} = 0$ to $\tilde{z} \approx -3200$. The CO_2 concentration profiles in both isotropic and anisotropic media closely follow the one-dimensional diffusion-only profile (44) at an early time of $\tilde{t} = 300$ (Figures 10a and 11a). The fingers are not readily observable at this time even though it is well beyond $\tilde{t}_c$. Small finger-like patterns become visible at around $\tilde{t}_{\min}$ (Figures 10b and 11b), which is also the time around which there is a substantial increase in the CO_2 dissolution rate. The average spacing of the fingers at $\tilde{t}_{\min}$
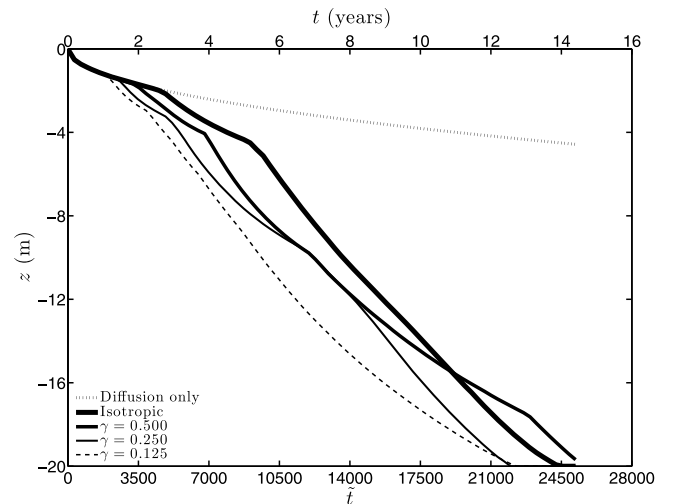

Figure 9. Location of the deepest front (DF) versus time. We define it as the deepest point where $\tilde{\omega}$ is greater than 0.001. Convection eventually accelerates the change in the DF. Anisotropy generally leads to larger fingering velocities, although the trend at later times becomes more unpredictable because of processes like finger splitting. Nevertheless, the DF reaches the bottom earlier in the two most anisotropic cases than it does in the isotropic case (Ra ≈ 3200).
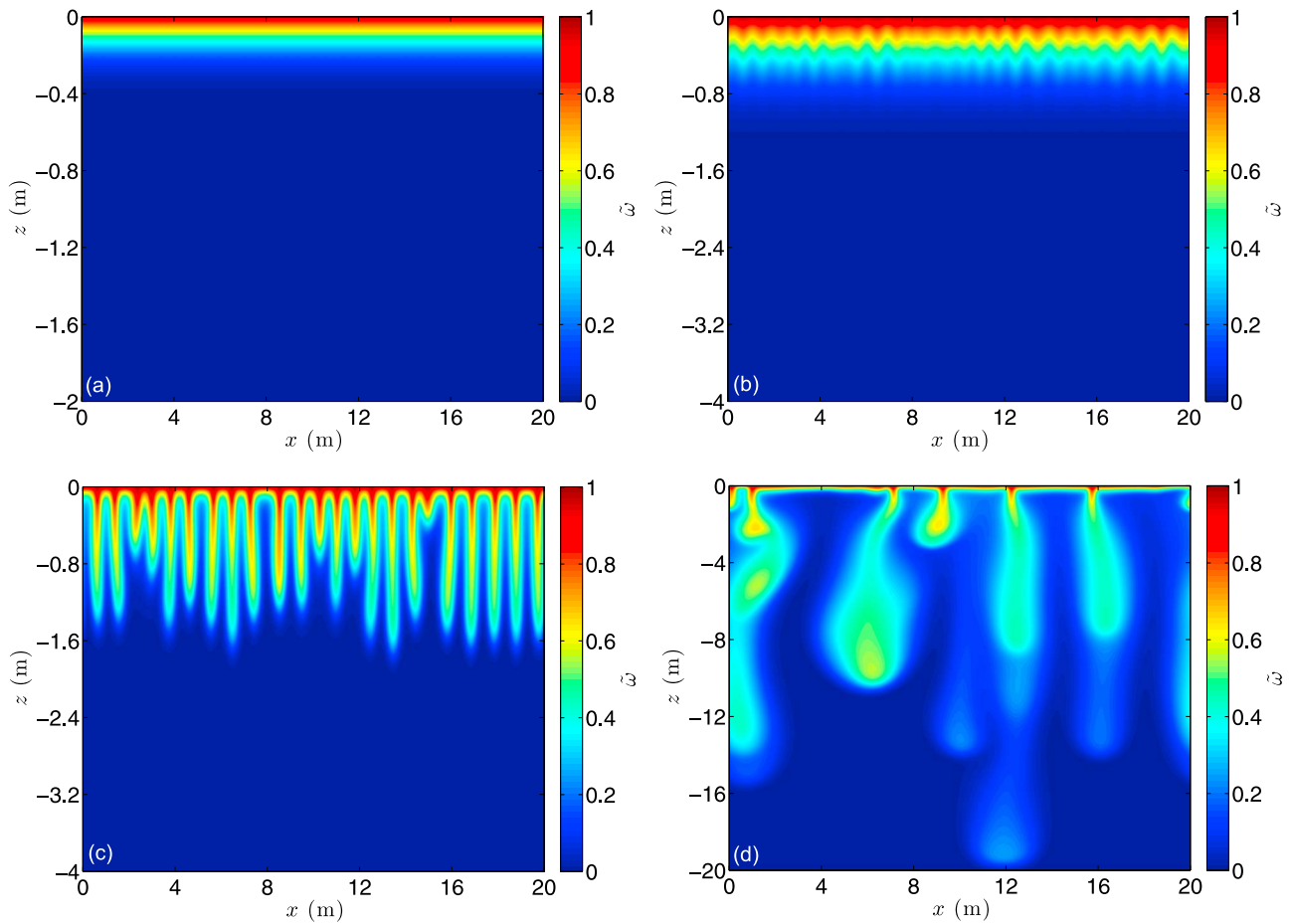
Figure 10. Snapshots of the CO$_2$ concentration profile in isotropic media: (a) $\tilde{t} = 300$, (b) $\tilde{t} = \tilde{t}_{\min}$, (c) $\tilde{t} = \tilde{t}_{\max}$, and (d) $\tilde{t} = 25000$. The top 10% of the porous domain is shown in Figure 10, the top 20% is shown in Figures 10b and 10c, and the entire domain is shown in Figure 10d (Ra ≈ 3200).

appears to be smaller in anisotropic media. However, the notion of an observable wavelength analogous to the critical wavelength is not applicable. Diffusive spreading, lateral movement, and merging of the fingers eventually distort the patterns and break the periodicity of the fingers in anisotropic media, as depicted in Figure 11c. These processes occur later in isotropic media. They alter the dynamics so that the fingers eventually emanate from only a few (time varying) discrete locations along the top. Figures 10d and 11d illustrate the finger splitting that may occur at later times. This process can accelerate the change in the DF as discussed in the previous section.

5. Conclusions

[35] We have presented and discussed results regarding the effect of permeability anisotropy on the onset and subsequent development of convection. We follow the same formulation widely used in the literature: isothermal, divergence-free flow in an idealized porous medium that has an impermeable bottom boundary, and a top boundary that remains constantly saturated with CO$_2$ while being impermeable only to convective fluid flow. We have focused on the situation where the vertical permeability k_z is fixed while the horizontal permeability k_h is increased. Our linear stability analysis shows that the critical time t_c and critical wavelength λ_c decrease

with increasing anisotropy. These findings are in agreement with previous results [*Xu et al.*, 2006]. The stability analysis reveals new insights about the mechanism through which the diffusion-only base state becomes more unstable. We have also performed high-resolution 2-D numerical simulations to study the behavior after onset. To the best of our knowledge, such simulations of anisotropic media are new in the CO$_2$ sequestration literature. The increased k_h from anisotropy allows fluid velocities to develop more rapidly and strengthens the intensity of the convection. We draw the following specific conclusions from this work.

[36] 1. Anisotropy causes all perturbation modes to become more unstable. It amplifies the perturbations via an exponential factor that grows in time and that is preferentially biased toward shorter wavelength modes. In this way it reduces t_c and λ_c.

[37] 2. Anisotropy increases the parity among the modes, making more of them almost equally unstable with the earliest-growing mode. This suggests that the notion of a critical wavelength becomes less meaningful with increasing anisotropy.

[38] 3. Anisotropy can substantially reduce the difference between t_c and the time $t_{\min}$ when the enhanced transport from convection becomes significant. Among other consequences, this is reflected in the more dramatic changes
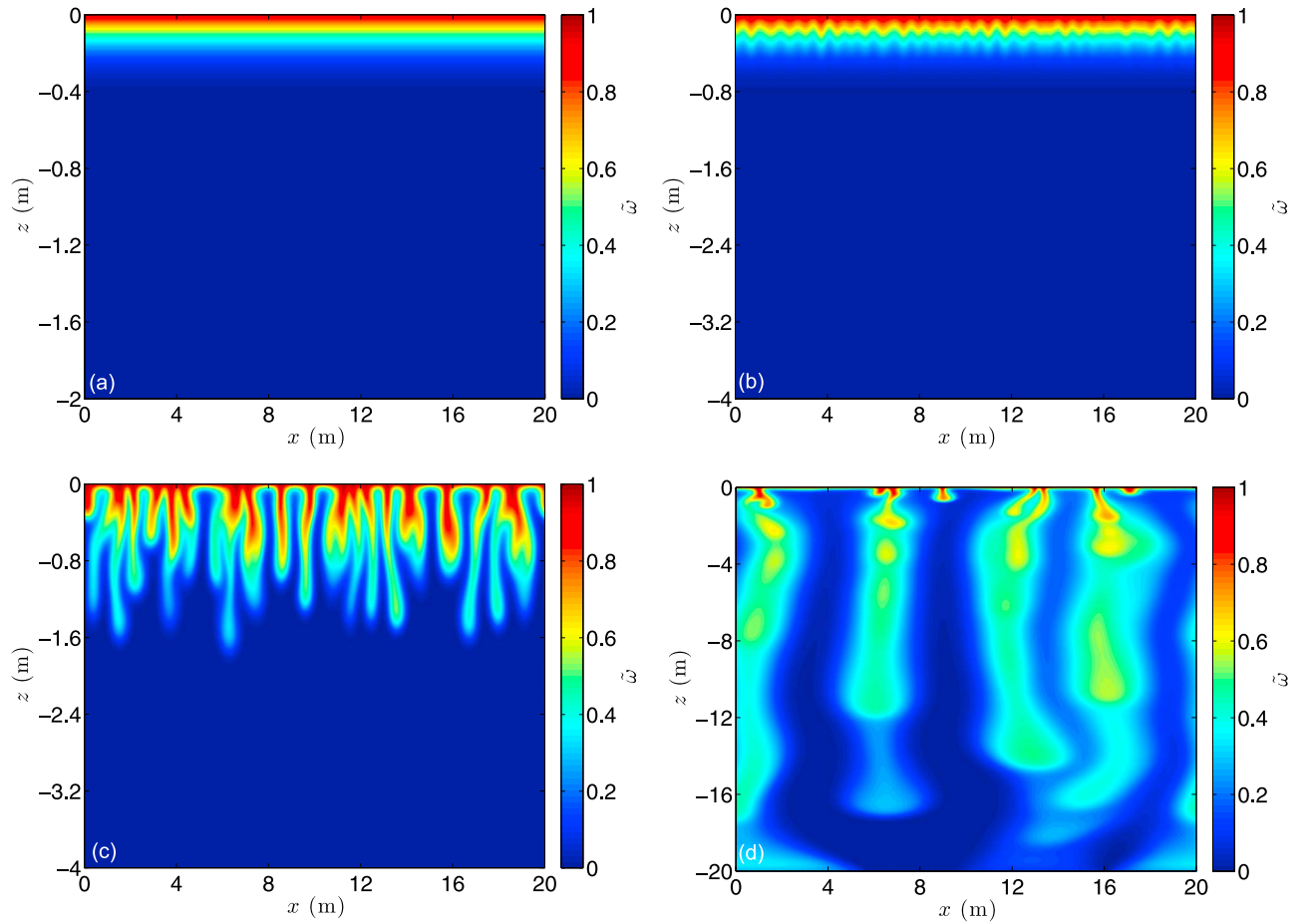
Figure 11. Snapshots of the CO$_2$ concentration profile for $\gamma = 0.125$: (a) $\tilde{t} = 300$, (b) $\tilde{t} = \tilde{t}_{\min}$, (c) $\tilde{t} = \tilde{t}_{\max}$, and (d) $\tilde{t} = 25000$. The top 10% of the porous domain is shown in Figure 11a, the top 20% is shown in Figures 11b and 11c, and the entire domain is shown in Figure 11d (Ra ≈ 3200).

undergone by the CO$_2$ concentration profile in anisotropic media.

[39]   4. Stronger convective flows permit higher mean CO$_2$ dissolution rates to be sustained for longer periods of time. This continues to be true after the fingers reach the bottom of the porous domain and even as the average saturation $\langle \tilde{\omega} \rangle$ begins to plateau. Compared to the isotropic case, a mildly anisotropic ($k_h = 8\ k_z$) medium is able to dissolve at least 50% more CO$_2$ by the end of our simulations.

[40]   5. The behavior at all times is strongly influenced by k_z. Its value across different aquifers in the world may vary by over 3 orders of magnitude. Ideally, high k_z formations should be chosen in order to maximize storage efficiency and minimize possibilities of CO$_2$ leakage [*IPCC*, 2005; *Weir et al.*, 1996; *Lindeberg and Wessel-Berg*, 1997; *Ennis-King et al.*, 2005; *Xu et al.*, 2006; *Riaz et al.*, 2006; *Firoozabadi and Cheng*, 2010]. Some formations may appear to be unsuitable for storage because of their low vertical permeability. If k_h is sufficiently high in these formations, they could still potentially be attractive storage sites as long as k_z is not too low.

Appendix A: Equation of State for Density

[41]   The linear constitutive equation in (6) can be justified from basic relations and definitions. The total volume V of

the fluid may be written in terms of the partial molar volumes of its components:

$$V = \bar{V}_1 n_1 + \bar{V}_2 n_2,$$

where $\bar{V}_1$ and $\bar{V}_2$ are the partial molar volumes of CO$_2$ and H$_2$O, respectively. The mole number of CO$_2$ is n_1 and that of H$_2$O is n_2. The partial molar volumes can be computed from an equation of state (EOS). We use the Cubic-plus-association (CPA) EOS developed by *Li and Firoozabadi* [2009], which has been shown to work well for CO$_2$-H$_2$O mixtures. The cubic part is from the Peng-Robinson (PR) EOS. It is customary to use volume shift parameters fitted to experimental data to improve the density prediction of the PR EOS and related equations of state. Accurate models for density are especially important for CO$_2$ sequestration, because the density difference between pure water and CO$_2$-saturated aqueous solutions is small (less than two percent). With the introduction of shift parameters, the total volume may then be expressed as

$$V = \bar{V}_1 n_1 + \bar{V}_2 n_2 + c_1 n_1 + c_2 n_2,$$

where c_1 is the shift parameter of CO$_2$ and c_2 is the shift parameter of H$_2$O. In this equation, $\bar{V}_1$ and $\bar{V}_2$ are the partial

molar volumes computed from the equation of state. In terms of the mass of each species, the volume is

$$V = \left(\frac{\bar{V}_1 + c_1}{M_1} \right) m_1 + \left(\frac{\bar{V}_2 + c_2}{M_2} \right) m_2,$$

with m_1 and m_2 being the mass of CO$_2$ and H$_2$O, respectively. We denote the molecular weight of CO$_2$ as M_1 and that of H$_2$O as M_2. The definition of ω is

$$\omega = \frac{m_1}{m_1 + m_2},$$

and that of ρ is

$$\rho = \frac{m_1 + m_2}{V}.$$

Combining them with the expression for the total volume yields

$$\rho = \frac{1}{\omega \left(\dfrac{\bar{V}_1 + c_1}{M_1} - \dfrac{\bar{V}_2 + c_2}{M_2} \right) + \dfrac{\bar{V}_2 + c_2}{M_2}}.$$

If we expand this about $\omega = 0$, we obtain the linear relation in (6):

$$\rho = \rho_0 (1 + \alpha \omega).$$

Here, ρ_0 is given by

$$\rho_0 = \frac{M_2}{\bar{V}_2 + c_2}.$$

The coefficient α is

$$\alpha = 1 - \rho_0 \left(\frac{\bar{V}_1 + c_1}{M_1} \right).$$

The temperature in our study is 30°C as mentioned in section 2.4. We find the partial molar volumes to be nearly invariant over a wide range of pressures and compositions at this temperature. The shift parameter of CO$_2$ is a constant, while that of H$_2$O is a function of only temperature [*Li and Firoozabadi*, 2009]. Thus, α and ρ_0 can be accurately approximated as being constants, and their values are 0.268 and 997.6 kg/m^3, respectively. We have compared predictions from (6) with experimental data for CO$_2$-saturated aqueous mixtures at 30°C over a pressure range from 10 to 100 bar. The theoretical values are, on average, about 0.2% different from experimental values [*Hebach et al.*, 2004].

Appendix B: Vertical Convective Flux Through the Top Boundary

[42] We show that the vertical convective flux between the CO$_2$-saturated aqueous layer along the top boundary and the CO$_2$ phase above it is negligible compared to the vertical diffusive flux. We present our arguments in dimensional terms for clarity. From a total mass balance and a species balance of CO$_2$ across the interface, we have, respectively,

$$\rho^G w^G = \rho^L w^L,$$

$$-\phi \rho^G D^G \frac{\partial \omega^G}{\partial z} + \omega^G \rho^G w^G = -\phi \rho^L D^L \frac{\partial \omega^L}{\partial z} + \omega^L \rho^L w^L,$$

where the superscript L denotes the aqueous layer, G denotes the supercritical CO$_2$ phase which is typically gas-like, and w is the vertical Darcy velocity. We can combine the above two equations to eliminate the velocity w^G to obtain

$$w^L = -\frac{\phi}{\omega^G - \omega^L} \left(D^L \frac{\partial \omega^L}{\partial z} - \frac{\rho^G}{\rho^L} D^G \frac{\partial \omega^G}{\partial z} \right).$$

If we use the fact that $\omega^G = 1$ throughout the entire CO$_2$ phase and that $\omega^L \ll 1$, the expression for w^L simplifies to

$$w^L = -\phi D^L \frac{\partial \omega^L}{\partial z},$$

which yields a convective flux J_c^L of

$$J_c^L = -\omega^L \phi \rho^L D^L \frac{\partial \omega^L}{\partial z}.$$

The mass fraction ω^L is 0.0428 in this study (see section 2.4), and therefore the magnitude of the convective flux is about only 4% of that of the diffusive flux. This justifies use of the no-flow condition at $z = 0$.

Appendix C: Derivation of the A$_\gamma$ Matrix

[43] We derive the elements of the matrices **B**, **C**, **D**, and **E** that form the time-dependent **A**$_\gamma$ matrix in (30). We start by substituting (28) and (29) into (26) and (27). We then multiply both sides of (26) by $\sin[(m - 1/2)\pi \tilde{z}/\text{Ra}]$ and both sides of (27) by $\sin(m\pi \tilde{z}/\text{Ra})$ and integrate both equations over $\tilde{z}$. Here, it is understood that $\{m \in \mathbb{N} : m \leq N\}$. The integral for the left-hand side of (26) is

$$\int_{-\text{Ra}}^{0} \sum_{n=1}^{N} \frac{d\hat{\omega}'_n}{d\tilde{t}} \sin\left[\left(n - \frac{1}{2}\right)\pi \frac{\tilde{z}}{\text{Ra}}\right] \sin\left[\left(m - \frac{1}{2}\right)\pi \frac{\tilde{z}}{\text{Ra}}\right] d\tilde{z}$$
$$= \frac{\text{Ra}}{2} \delta_{mn} \frac{d\hat{\omega}'_n}{d\tilde{t}} = \frac{\text{Ra}}{2} \frac{d\hat{\omega}'_m}{d\tilde{t}}. \qquad (\text{C1})$$

For the first term on the right-hand side of (26), we take the time derivative of the profile $\tilde{\omega}_{\text{base}}$ given in (16):

$$\frac{\partial \tilde{\omega}_{\text{base}}}{\partial \tilde{z}} = \frac{2}{\text{Ra}} \sum_{l=1}^{\infty} \cos\left[\left(l - \frac{1}{2}\right)\frac{\pi \tilde{z}}{\text{Ra}}\right] \exp\left\{-\left[\left(l - \frac{1}{2}\right)\frac{\pi}{\text{Ra}}\right]^2 \tilde{t}\right\}.$$

For convenience, let us temporarily denote the expression inside the exponential as $f(l, \tilde{t}) = -[(l - 1/2)\pi/R]^2 \tilde{t}$. Then the integral of the first term on the right-hand side is

$$-\frac{2}{\text{Ra}} \int_{-\text{Ra}}^{0} \sum_{n=1}^{N} \sum_{l=1}^{\infty} \hat{w}'_n \exp[f(l, \tilde{t})] \sin\left(n\pi \frac{\tilde{z}}{\text{Ra}}\right) \cos\left[\left(l - \frac{1}{2}\right)\frac{\pi \tilde{z}}{\text{Ra}}\right]$$
$$\cdot \sin\left[\left(m - \frac{1}{2}\right)\frac{\pi \tilde{z}}{\text{Ra}}\right] d\tilde{z}.$$

Using the formula $\cos(a)\sin(b) = [\sin(a + b) - \sin(a - b)]/2$, this integral becomes

$$\frac{1}{\text{Ra}} \int_{-\text{Ra}}^{0} \sum_{n=1}^{N} \sum_{l=1}^{\infty} \hat{w}'_n \exp[f(l, \tilde{t})] \sin\left(n\pi \frac{\tilde{z}}{\text{Ra}}\right)$$
$$\cdot \left\{ \sin\left[(l - m)\frac{\pi \tilde{z}}{\text{Ra}}\right] - \sin\left[(l + m - 1)\frac{\pi \tilde{z}}{\text{Ra}}\right] \right\} d\tilde{z}.$$

Writing out the explicit dependence of the exponential term on l and $\tilde{t}$ and evaluating the integral yields

$$\frac{1}{2}\sum_{n=1}^{N}\left[\delta_{n,l-m}-\delta_{n,l+m-1}\right]\exp\left\{-\left[\left(l-\frac{1}{2}\right)\frac{\pi}{\text{Ra}}\right]^2\tilde{t}\right\}\hat{w}'_n,$$

which leads to

$$\frac{1}{2}\sum_{n=1}^{N}\left(\exp\left\{-\left[\left(m+n-\frac{1}{2}\right)\frac{\pi}{\text{Ra}}\right]^2\tilde{t}\right\}\right.$$
$$\left.-\exp\left\{-\left[\left(n-m+\frac{1}{2}\right)\frac{\pi}{\text{Ra}}\right]^2\tilde{t}\right\}\right)\hat{w}'_n. \quad (C2)$$

The integrals for the second and third terms on the right-hand side of (26) may be evaluated together to obtain

$$-\frac{\text{Ra}}{2}\left\{\left[\left(n-\frac{1}{2}\right)\frac{\pi}{\text{Ra}}\right]^2+\gamma\tilde{s}^2\right\}\delta_{mn}\hat{\omega}'_n$$
$$=-\frac{\text{Ra}}{2}\left\{\left[\left(m-\frac{1}{2}\right)\frac{\pi}{\text{Ra}}\right]^2+\gamma\tilde{s}^2\right\}\hat{\omega}'_m. \quad (C3)$$

Following a similar procedure for the two terms on the left-hand side of (27), we have

$$-\frac{\text{Ra}}{2}\left[\left(\frac{n\pi}{\text{Ra}}\right)^2+\tilde{s}^2\right]\delta_{mn}\hat{w}'_n=-\frac{\text{Ra}}{2}\left[\left(\frac{m\pi}{\text{Ra}}\right)^2+\tilde{s}^2\right]\hat{w}'_m. \quad (C4)$$

The integral of the right-hand side of (27) is

$$\tilde{s}^2\int_{-\text{Ra}}^{0}\sum_{n=1}^{N}\hat{\omega}'_n\sin\left[\left(n-\frac{1}{2}\right)\pi\frac{\tilde{z}}{\text{Ra}}\right]\sin\left(m\pi\frac{\tilde{z}}{\text{Ra}}\right)d\tilde{z}.$$

To compute this integral, we use the formula $\sin(a)\sin(b) = [\cos(a-b)-\cos(a+b)]/2$ to find that

$$\tilde{s}^2\int_{-\text{Ra}}^{0}\sum_{n=1}^{N}\hat{\omega}'_n\sin\left[\left(n-\frac{1}{2}\right)\pi\frac{\tilde{z}}{\text{Ra}}\right]\sin\left(m\pi\frac{\tilde{z}}{\text{Ra}}\right)d\tilde{z}$$
$$=\sum_{n=1}^{N}\frac{\tilde{s}^2\text{Ra}}{\pi}(-1)^{m+n}\frac{4m}{4m^2-(2n-1)^2}\hat{\omega}'_n. \quad (C5)$$

Combining (C1) with (C2) and (C3), we have

$$\frac{d\hat{\omega}'_m}{d\tilde{t}}=-\left\{\left[\left(m-\frac{1}{2}\right)\frac{\pi}{\text{Ra}}\right]^2+\gamma\tilde{s}^2\right\}\hat{\omega}'_m$$
$$+\frac{1}{\text{Ra}}\sum_{n=1}^{N}\left(\exp\left\{-\left[\left(m+n-\frac{1}{2}\right)\frac{\pi}{\text{Ra}}\right]^2\tilde{t}\right\}\right.$$
$$\left.-\exp\left\{-\left[\left(n-m+\frac{1}{2}\right)\frac{\pi}{\text{Ra}}\right]^2\tilde{t}\right\}\right)\hat{w}'_n.$$

Combining (C4) with (C5), we get

$$-\frac{1}{2}\left[\left(\frac{m\pi}{\text{Ra}}\right)^2+\tilde{s}^2\right]\hat{w}'_m=\sum_{n=1}^{N}\frac{\tilde{s}^2}{\pi}(-1)^{m+n}\frac{4m}{4m^2-(2n-1)^2}\hat{\omega}'_n.$$

These equations apply for a particular value of m. If we consider all allowable values of m, we obtain

$$\frac{d\boldsymbol{\omega}_\gamma}{d\tilde{t}}=\mathbf{B}\boldsymbol{\omega}_\gamma+\mathbf{C}\mathbf{w}_\gamma, \quad (C6)$$

$$\mathbf{D}\mathbf{w}_\gamma=-\mathbf{E}\boldsymbol{\omega}_\gamma, \quad (C7)$$

where $\boldsymbol{\omega}_\gamma$ is the column vector $(\hat{\omega}'_1, \hat{\omega}'_2, \ldots, \hat{\omega}'_N)^T$ and $\mathbf{w}_\gamma$ is the column vector $(\hat{w}'_1, \hat{w}'_2, \ldots, \hat{w}'_N)^T$. The elements of the matrices are

$$B_{mn}=-\left\{\left[\left(n-\frac{1}{2}\right)\frac{\pi}{\text{Ra}}\right]^2+\gamma\tilde{s}^2\right\}\delta_{mn},$$

$$C_{mn}=\frac{1}{\text{Ra}}\left(\exp\left\{-\left[\left(m+n-\frac{1}{2}\right)\frac{\pi}{\text{Ra}}\right]^2\tilde{t}\right\}\right.$$
$$\left.-\exp\left\{-\left[\left(n-m+\frac{1}{2}\right)\frac{\pi}{\text{Ra}}\right]^2\tilde{t}\right\}\right),$$

$$D_{mn}=\frac{1}{2}\left[\left(\frac{n\pi}{\text{Ra}}\right)^2+\tilde{s}^2\right]\delta_{mn},$$

$$E_{mn}=\frac{\tilde{s}^2}{\pi}(-1)^{m+n}\frac{4m}{4m^2-(2n-1)^2}.$$

We can substitute (C7) into (C6) to obtain (30), where $\mathbf{A}_\gamma=\mathbf{B}-\mathbf{C}\mathbf{D}^{-1}\mathbf{E}$.

References

Bell, W. W. (2004), *Special Functions for Scientists and Engineers*, Dover, Mineola, N. Y.

Bestehorn, M. (1993), Phase and amplitude instabilities for Bénard-Marangoni convection in fluid layers with large aspect ratio, *Phys. Rev. E*, *48*, 3622–3634, doi:10.1103/PhysRevE.48.3622.

Bestehorn, M., and P. Colinet (2000), Bénard-Marangoni convection of a binary mixture as an example of an oscillatory bifurcation under strong symmetry-breaking effects, *Physica D*, *145*, 84–109, doi:10.1016/S0167-2789(00)00111-1.

Caltagirone, J. P. (1980), Stability of a saturated porous layer subject to a sudden rise in surface temperature: Comparison between the linear and energy methods, *Q. J. Mech. Appl. Math.*, *33*, 47–58, doi:10.1093/qjmam/33.1.47.

Carslaw, H. S., and J. C. Jaeger (1986), *Conduction of Heat in Solids*, Oxford Univ. Press, Oxford, U. K.

Crank, J. (1980), *Mathematics of Diffusion*, 2nd ed., Oxford Univ. Press, Oxford, U. K.

Doering, C. R., and P. Constantin (1998), Bounds for heat transport in a porous layer, *J. Fluid Mech.*, *376*, 263–296, doi:10.1017/S002211209800281X.

Elenius, M. T., and K. Johannsen (2012), On the time scales of nonlinear instability in miscible displacement porous media flow, *Comput. Geosci.*, doi:10.1007/s10596-012-9294-2, in press.

Ennis-King, J., and L. Paterson (2005), Role of convective mixing in the long-term storage of carbon dioxide in deep saline formations, *SPE J.*, *10*(3), 349–356, doi:10.2118/84344-PA.

Ennis-King, J., I. Preston, and L. Paterson (2005), Onset of convection in anisotropic porous media subject to a rapid change in boundary conditions, *J. Phys. Fluids*, *17*(8), 084107, doi:10.1063/1.2033911.

Firoozabadi, A., and P. Cheng (2010), Prospects for subsurface CO_2 sequestration, *AIChE*, *56*(6), 1398–1405, doi:10.1002/aic.12287.

Foster, T. (1965), Stability of a homogeneous fluid cooled uniformly from above, *J. Phys. Fluids*, *8*(7), 1249–1257, doi:10.1063/1.1761393.

Hassanzadeh, H., M. Pooladi-Darvish, and D. W. Keith (2007), Scaling behavior of convective mixing, with application to geological storage of CO_2, *AIChE*, *53*(5), 1121–1131, doi:10.1002/aic.11157.

Hebach, A., A. Oberhof, and N. Dahmen (2004), Density of water + carbon dioxide at elevated pressures: Measurements and correlation, *J. Chem. Eng. Data*, *49*, 950–953, doi:10.1021/je034260i.

Hidalgo, J. J., and J. Carrera (2009), Effect of dispersion on the onset of convection during CO$_2$ sequestration, *J. Fluid Mech.*, *640*, 441–452, doi:10.1017/S0022112009991480.

Hong, J., and M. Kim (2008), Effect of anisotropy of porous media on the onset of buoyancy-driven convection, *Transp. Porous Media*, *72*, 241–253, doi:10.1007/s11242-007-9147-y.

Intergovernmental Panel on Climate Change (IPCC) (2005), Special report on carbon dioxide capture and storage, World Meteorol. Organ., Geneva, Switzerland.

Kneafsey, T., and K. Pruess (2010), Laboratory flow experiments for visualizing carbon dioxide-induced, density-driven brine convection, *Transp. Porous Media*, *82*, 123–139, doi:10.1007/s11242-009-9482-2.

Li, Z., and A. Firoozabadi (2009), Cubic-plus-association equation of state for water-containing mixtures: Is "cross association" necessary?, *AIChE*, *55*(7), 1803–1813, doi:10.1002/aic.11784.

Lick, W. (1965), The instability of a fluid layer with time-dependent heating, *J. Fluid Mech.*, *3*, 565–576, doi:10.1017/S0022112065000332.

Lindeberg, E., and D. Wessel-Berg (1997), Vertical convection in an aquifer column under a gas cap of CO$_2$, *Energy Convers. Manage.*, *38*, S229–S234, doi:10.1016/S0196-8904(96)00274-9.

Mutoru, J., A. Leahy-Dios, and A. Firoozabadi (2011), Modeling infinite dilution and Fickian diffusion coefficients of carbon dioxide in water, *AIChE*, *57*(6), 1617–1627, doi:10.1002/aic.12361.

Pau, G. S. H., J. B. Bell, K. Pruess, A. S. Almgren, M. J. Lijewski, and K. Zhang (2010), High-resolution simulation and characterization of density-driven flow in CO$_2$ storage in saline aquifers, *Adv. Water Resour.*, *33*, 443–455, doi:10.1016/j.advwatres.2010.01.009.

Pruess, K., and K. Zhang (2008), Numerical modeling studies of the dissolution-diffusion-convection process during CO$_2$ storage in saline aquifers, technical report, Lawrence Berkeley Natl. Lab., Berkeley, Calif.

Rapaka, S., S. Chen, R. J. Pawar, P. H. Stauffer, and D. Zhang (2008), Non-modal growth of perturbations in density-driven convection in porous media, *J. Fluid Mech.*, *609*, 285–303, doi:10.1017/S0022112008002607.

Rapaka, S., R. J. Pawar, P. H. Stauffer, D. Zhang, and S. Chen (2009), Onset of convection over a transient base-state in anisotropic and layered porous media, *J. Fluid Mech.*, *641*, 227–244, doi:10.1017/S0022112009991479.

Riaz, A., M. Hesse, H. A. Tchelepi, and F. M. Orr (2006), Onset of convection in a gravitationally unstable diffusive boundary layer in porous media, *J. Fluid Mech.*, *548*, 87–111, doi:10.1017/S0022112005007494.

Roache, P. J. (1998), *Fundamentals of Computational Fluid Dynamics*, 3rd ed., Hermosa, Albuquerque, N. M.

Rongy, L., K. B. Haugen, and A. Firoozabadi (2012), Mixing from Fickian diffusion and natural convection in binary non-equilibrium fluid phases, *AIChE J.*, *58*(5), 1336–1345, doi:10.1002/aic.12685.

Slim, A. C., and T. S. Ramakrishan (2010), Onset and cessation of time-dependent, dissolution-driven convection in porous media, *J. Phys. Fluids*, *22*, 124103, doi:10.1063/1.3528009.

Swarztrauber, P. N. (1982), Vectorizing the FFTs, in *Parallel Computations*, pp. 51–83, Academic, New York.

Tan, C. T., and G. M. Homsy (1988), Simulation of nonlinear viscous fingering in miscible displacement, *J. Phys. Fluids*, *31*(6), 1330–1338, doi:10.1063/1.866726.

Thess, A., and S. A. Orszag (1995), Surface-tension-driven Bénard convection at infinite Prandtl number, *J. Fluid Mech.*, *283*, 201–230, doi:10.1017/S002211209500228X.

Weir, G. J., S. P. White, and W. M. Kissling (1996), Reservoir storage and containment of greenhouse gases, *Transp. Porous Media*, *23*, 37–60, doi:10.1007/BF00145265.

Xie, Y., C. Simmons, and D. Werner (2011), Speed of free convective fingering in porous media, *Water Resour. Res.*, *47*, W11501, doi:10.1029/2011WR010555.

Xu, X., S. Chen, and D. Zhang (2006), Convective stability analysis of the long-term storage of carbon dioxide in deep saline aquifers, *Adv. Water Resour.*, *29*, 397–407, doi:10.1016/j.advwatres.2005.05.008.

Yang, C., and Y. Gu (2006), Accelerated mass transfer of CO$_2$ in reservoir brine due to density-driven natural convection at high pressures and elevated temperatures, *Ind. Eng. Chem. Res.*, *45*, 2430–2436, doi:10.1021/ie050497r.